Journal of Fluids and Structures 147 (2026) 104663

Contents lists available at ScienceDirect

Journal of Fluids and Structures

journal homepage: www.elsevier.com/locate/yjfls

Nonlinear wave interactions with point-absorber WEC arrays using qaleFOAM

Yi Zhang [a,b], Qian Li [a,c], Shiqiang Yan [a,*], Qingwei Ma [a]

[a] School of Science and Technology, City St George's, University of London, London, EC1V 0HB, UK
[b] School of Engineering, The University of Manchester, Manchester, M13 9PL, UK
[c] EDF UK R&D, Nova North, 11 Bressenden Place, London, SW1E 5BY, UK

ARTICLE INFO

Keywords:
WEC
Array
Power performance
Nonlinear interaction
q-factor
qaleFOAM

ABSTRACT

This paper extends a hybrid model qaleFOAM to assess the nonlinear interaction of waves with an array of point-absorber wave energy converters (WECs). The hybrid model uses an adaptive one-way coupling strategy, combining a two-phase Navier–Stokes (NS) solver interDyMFoam with the fully nonlinear potential theory (FNPT)-based solver QALE-FEM. To minimise the computational cost, an improved wave absorbing technique is adopted to absorb the undesirable reflected waves at the inlet/outlet boundary of the NS domain instead of using the conventional relaxation zone technique. The model is first assessed against available single-buoy benchmark data, and then applied to regular head-wave cases involving CorPower-type buoys arranged in line arrays. The effects of wave steepness, PTO damping and non-dimensional array spacing are examined. For the two-buoy cases, increasing wave steepness increases the mean surge and pitch drifts and enhances the asymmetry of the instantaneous absorbed power, while reducing the normalised first-harmonic motion amplitudes. Increasing PTO damping reduces the heave response but increases restraint forces and power fluctuations, and may promote overtopping under the studied conditions. For the three-buoy cases, the *q*-factor and the absorbed power of each buoy vary non-monotonically with non-dimensional spacing d/λ, with the minimum *q*-factor observed at $d/\lambda \approx 0.5$. Shorter waves produce stronger shielding effects on the middle and rear buoys, affecting both hydrodynamic loads and tether-force fluctuations. These results demonstrate that, within the tested configurations, nonlinear wave effects, PTO damping and array spacing can influence motion response, power absorption and load distribution among buoys.

1. Introduction

Ocean waves contain a huge amount of energy. To extract energy from waves, various concepts of wave energy converters (WECs) have been developed (Babarit, 2015; Falcão, 2010; Falnes, 2007), such as oscillating water columns, oscillating bodies and overtopping devices. Among them, point absorbers have gained wide attention since the 1970s (Budal and Falnes, 1975) due to their simple construction. In a wave energy farm, point-absorber WECs are usually deployed in arrays using a specific configuration to extract large amounts of wave energy in an economical manner. When a WEC is placed in an array, the scattered and radiated waves from surrounding WECs may significantly affect the motions of the WEC, particularly when the WECs are closely spaced and/or in relatively

* Corresponding author.
E-mail address: Shiqiang.Yan.1@city.ac.uk (S. Yan).

https://doi.org/10.1016/j.jfluidstructs.2026.104663
Received 21 April 2026; Received in revised form 9 July 2026; Accepted 3 August 2026
Available online 8 August 2026

shorter wave scenarios (Babarit, 2013). Consequently, the power extraction performance of the WEC in the array is different from that of an isolated device. Therefore, it is essential to gain an in-depth understanding of the hydrodynamic interaction in the WEC array for evaluating the power extraction performance and optimising the configuration of WEC arrays to minimise the levelized cost of energy (LCOE) of the wave energy farm.

Early work on analysing the power performance of the WEC array can be traced back to the pioneering work done by Budal (1977), Evans (1979) and Falnes (1980), who developed analytical solutions for the maximum absorbed power by arrays of axisymmetric heaving devices in unidirectional regular waves using the linear potential flow theory and the point-absorber approximation. Apart from the analytical approaches, the linearised diffraction-radiation analysis based on the boundary element method (BEM) is more commonly applied to WECs with different geometries and/or non-optimal states, e.g., Child and Venugopal (2010), Wolgamot et al. (2012) and Liu et al. (2022). More detailed reviews can be found in Folley et al. (2012), Babarit (2013) and He et al. (2023), which present a range of methodologies for analysing the hydrodynamic and power performance of WEC arrays and summarise the main findings including but not limited to (1) hydrodynamic interaction among WECs are important; (2) their influence on array power performance depends on wave frequency (or wavelength) and array configuration, including device spacing and mooring arrangement; (3) wave direction may significantly affect the power capture performance of the array. These findings provide a good foundation for the design and deployment of the WEC array. However, the theoretical limitations of the linear methods adopted in existing studies restrict their applicability to cases involving small WEC motions induced by small-amplitude waves. In certain scenarios, such as when WECs are exposed to steep incoming waves and/or operate at or near resonance, their hydrodynamic responses can be significantly affected by nonlinear effects, including wave nonlinearity, large-amplitude body motions, viscous and turbulent effects, slamming, and wave overtopping. In such cases, linear or weakly-nonlinear models may lead to considerable numerical uncertainty and may not provide reliable predictions. Consequently, nonlinear hydrodynamic studies on wave interaction with WEC arrays are still scarce in the open literature.

Although a range of numerical approaches have been proposed for simulating WECs, as reviewed by Li and Yu (2012), Wolgamot and Fitzgerald (2015), Davidson and Costello (2020), most studies still rely on the above-mentioned linear or weakly nonlinear diffraction-radiation models (e.g., Babarit et al., 2012). However, to capture nonlinear effects, especially small-scale viscous and turbulent effects, violent slamming and wave overtopping, CFD models based on Navier–Stokes (NS) equations may be necessary. However, NS-based models are extremely time-consuming and, in many cases, practically prohibitive for simulating wave interactions with WEC arrays. Their high computational cost mainly arises from: (1) fine temporal/spatial discretization required to capture the small-scale physics and ensure solution convergence, and (2) the requirement of large computational domain to facilitate the wave generation, either through a numerical wavemaker or proper wave inlet boundary conditions (Jacobsen et al., 2012; Windt et al., 2019), as well as wave absorption using relaxation or damping zones (Yan et al., 2020). The computational demand increases further when multiple WECs are included, not only because a larger domain is required to accommodate the array, but also because of the growing complexity of mesh handling. This is particularly challenging when mesh morphing is used, as the computational mesh may become more severely distorted by the relative motions of multiple WECs. Consequently, applications of NS-based models have so far been focused primarily on single WEC devices. Only a limited number of studies, such as McCallum (2017), Devolder et al. (2017) have reported preliminary investigations of multi-WEC systems, providing interesting findings from free-decay and regular wave tests of arrays with two or five devices. More recently, Chen et al. (2025) conducted a comparative study of a taut-moored point-absorber WEC array, showing that a potential-flow based BEM model with viscous damping can reasonably predict the linear heave response and power absorption, while a CFD model captures additional nonlinear effects, such as surge slow-drift and higher-order pitch harmonics. These findings highlight the need for further investigation into the nonlinear hydrodynamic interactions within WEC arrays.

In this paper, the nonlinear hydrodynamic response of a WEC array in regular waves is investigated using a numerical wave tank (NWT) based on the two-phase NS solver OpenFOAM/interDyMFoam to capture violent wave impacts, overtopping and large-amplitude motions. To minimise the computational domain thereby improve the computing efficiency, two key techniques associated with wave generation and absorption are employed. At the outlet of the NWT, an improved wave absorbing technique is adopted. Unlike the relaxation or damping zone techniques widely used in the traditional NS simulation, which generally require an additional computational domain of 1–2 wavelengths to reduce outlet wave reflections, this approach requires no extra computational domain, as the wave absorption is imposed directly at the boundary instead of within an additional relaxation zone. At the inlet, the NWT is

Table 1
Comparison of the present study with relevant CFD/BEM studies on single WECs and WEC arrays.

Reference	Numerical model	Boundary treatment	Dynamic mesh	Body configuration
Li et al. (2018)	qaleFOAM	Relaxation zones at the inlet/outlet	N/A	Fixed horizontal cylinder
Yan et al. (2020)	qaleFOAM	Relaxation zone at the inlet, improved wave-absorbing technique at the outlet	Mesh morphing	Single WEC
Devolder et al. (2017)	OpenFOAM	Active wave absorption boundary using IHFOAM	Arbitrary mesh interfaces (AMIs)	WEC arrays
Liu et al. (2022)	BEM	Radiation condition	N/A	WEC arrays
Chen et al. (2025)	OpenFOAM	Active wave absorption boundary using IHFOAM	Overset mesh	WEC arrays
Present study	qaleFOAM	Improved wave-absorbing techniques at the inlet/outlet	Improved mesh-morphing	WEC arrays

coupled with the FNPT solver QALE-FEM (Ma and Yan, 2006) via an adaptive one-way coupling strategy. Based on our existing hybrid model qaleFOAM (Li et al., 2018; Yan et al., 2020), the improved wave absorbing technique is further extended to the inlet boundary to absorb body-reflected waves, replacing the conventional transition or relaxation zone techniques. The NS solver employs a dynamic mesh technique to ensure that the body-fitted computational mesh conforms to the motions of the floating bodies. To address the potential mesh distortion arising in simulations with multiple floating bodies, an improved interpolation algorithm for nodal displacements is developed in this paper. The main contributions of this paper are: (i) extension of the qaleFOAM framework to multi-buoy arrays, (ii) use of the boundary-based wave absorber at the inlet/outlet boundaries to replace long transition/relaxation zones, (iii) an improved mesh-morphing interpolation function, and (iv) the parametric study of nonlinear array behaviour. Table 1 provides a concise comparison distinguishing the present work from previous qaleFOAM studies and relevant recent CFD/BEM studies on WECs and WEC arrays.

The remainder of this paper is organized as follows. Section 2 introduces the mathematical formulations and numerical methods implemented in qaleFOAM, the coupling between the solvers, and the power performance evaluation of WECs. Section 3 describes the numerical set-up, the mesh convergence and validation tests. Section 4 discusses the nonlinear interactions between regular waves and multiple WECs under various scenarios, including different WEC arrangements, wave steepnesses, and PTO damping coefficients. Finally, the main conclusions are given in Section 5.

2. Mathematical formulation

2.1. Numerical wave tank

In the numerical wave tank, denoted by Ω_{NS}, the two-phase NS solver interDyMFoam is used to simulate the water and air flow properties by the finite volume method (FVM). The volume of fluid (VOF) technique is adopted to identify the free surface. The incompressible Reynolds Averaged Navier-Stokes (RANS) equations are written in an arbitrary Lagrangian–Eulerian (ALE) form as:

$$\nabla \cdot \mathbf{u} = 0 \tag{1}$$

$$\frac{\partial(\rho\mathbf{u})}{\partial t} + \nabla \cdot \left[\rho\left(\mathbf{u} - \mathbf{u}_g\right)\mathbf{u}^{\mathrm{T}}\right] = -\nabla p + \nabla \cdot \boldsymbol{\tau} + \rho\mathbf{g} \tag{2}$$

where $\mathbf{u}$ is the fluid velocity; $\mathbf{u}_g$ is the grid velocity; ρ is the fluid density; p is the pressure; $\boldsymbol{\tau} = \mu_{\mathrm{eff}}\left[\nabla\mathbf{u} + (\nabla\mathbf{u})^{\mathrm{T}}\right]$ is the viscous stress tensor, in which $\mu_{\mathrm{eff}} = \mu + \mu_t$ denotes the effective dynamic viscosity, including the molecular viscosity μ and the turbulent viscosity μ_t; and $\mathbf{g} = (0, 0, -g)$ denotes the gravitational acceleration vector. Note that turbulence effects are not dominant in this study, as the flow considered here is characterized by a moderate Keulegan-Carpenter number. Thus, only the laminar model is employed.

The free surface is identified by the VOF method, and a volume fraction $\alpha \in [0, 1]$ is defined, where $\alpha = 0$ and $\alpha = 1$ denote the air phase and water phase respectively, and α between 0 and 1 represents the interface. The volume fraction α follows the convection equation:

$$\frac{\partial\alpha}{\partial t} + \nabla \cdot \left(\mathbf{u} - \mathbf{u}_g\right)\alpha + \nabla \cdot \mathbf{u}_c\alpha(1 - \alpha) = 0 \tag{3}$$

On the left-hand side of Eq. (3), the last term is an artificial interface compression term, which is added to prevent a blur of the interface. $\mathbf{u}_c$ denotes the compression velocity, which is perpendicular to the interface and can be expressed as $\mathbf{u}_c = c_\alpha|\mathbf{u}|\frac{\nabla\alpha}{|\nabla\alpha|}$, where c_α is a user-specified compression factor controlling the interface compression strength. Further details have been given in Berberović et al. (2009). Using the volume fraction α, the local fluid properties (e.g., the fluid density and dynamic viscosity) in a cell can be expressed as a mixture of water and air, i.e.,

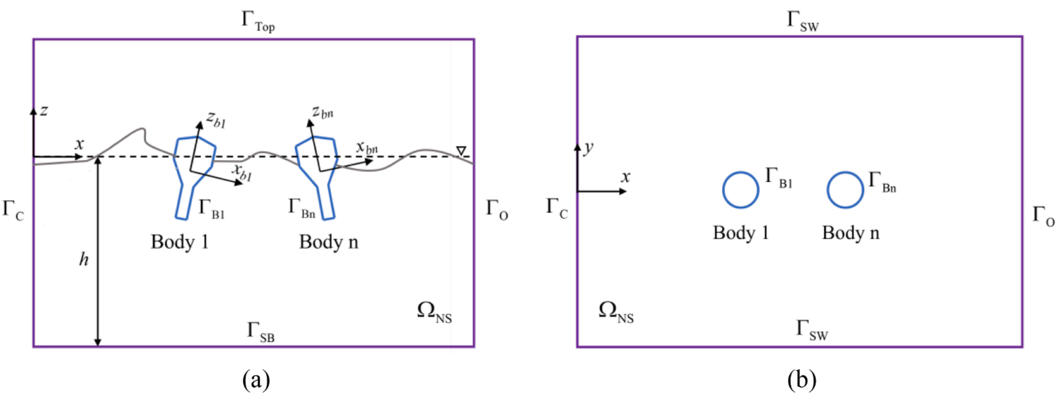

Fig. 1. Sketch of the numerical wave tank in the NS domain. (a) Side view; (b) Plane view.

$$\rho = \alpha\rho_w + (1-\alpha)\rho_a \tag{4}$$

$$\mu = \alpha\mu_w + (1-\alpha)\mu_a \tag{5}$$

in which the subscripts 'w' and 'a' denote water and air, respectively.

As shown in Fig. 1, Ω_{NS} covers a small zone around the bodies and is bounded by an inlet boundary Γ_C at its left side, an outlet boundary Γ_O at its right side, a pressure inlet/outlet boundary Γ_{Top} on the top, in which the atmospheric pressure is imposed, several body boundaries Γ_{B1}, Γ_{Bn}, in which a no-slip velocity condition and a fixed-flux pressure condition are imposed, a slip wall boundary Γ_{SB} on the seabed, and two slip vertical walls Γ_{SW} on the front and back sides. Two Cartesian coordinate systems are defined here. One is the space-fixed coordinates $Oxyz$ with the origin O at the still water surface and the z-axis pointing upwards, and the other is the body-fixed coordinates $O_bx_by_bz_b$ with the origin O_b located at the centre of gravity of the body. The water depth h is assumed to be constant.

The outlet boundary Γ_O is expected to allow a free propagation of the incoming wave. Otherwise, undesirable reflected waves will be generated and propagate back towards floating bodies, influencing the accuracy of the simulation. The relaxation zone technique is usually implemented to avoid the reflected waves from Γ_O (e.g., Aliyar et al., 2022; Gong et al., 2020; Jacobsen et al., 2012; Li et al., 2018). However, such technique requires a large computational domain to accommodate the relaxation zone, as mentioned in Introduction. In this study, an improved wave absorbing technique is implemented based on the concept of providing a reliable prediction of the local fluid velocity at Γ_O and specifying it as the velocity boundary condition. A detailed description about the technique has been provided in Yan et al. (2020) but a brief introduction is given here for completeness. The technique is derived from the linear regular wave theory assuming the wave elevation $\eta(t)$ at Γ_O can be described as:

$$\eta(t) = A\cos(\psi(t)) \tag{6}$$

where A and ψ are the wave amplitude and wave phase, and the corresponding horizontal velocity $u_h(t)$ below the free surface can be written as:

$$u_h(t) = \omega\frac{\cosh(k(z+h))}{\sinh(kh)}\eta(t) \tag{7}$$

in which ω and k denote the wave frequency and wave number. By sampling the instantaneous wave elevation $\eta(t)$ at Γ_O, one can determine $u_h(t)$. However, the wave at Γ_O may contain significant nonlinearity and consist of different wave components. In order to incorporate these, one may assume that the above linear relation stands in a short duration at the scale of time step size. By introducing instantaneous wave information, including the instantaneous wave frequency and wave number, Eq. (7) can be extended to:

$$u_h(t) = \widetilde{\omega}\frac{\cosh(\widetilde{k}(z'+h))}{\sinh(\widetilde{k}h)}\eta(t) \tag{8}$$

where $\widetilde{\omega}$ and $\widetilde{k}$ represent the instantaneous wave frequency and wave number at Γ_O, and $z' = \frac{z-\eta}{\eta+h}h$. $\widetilde{\omega}$ can be tracked by the extended Kalman filter (EKF) using the instantaneous wave elevation $\eta(t)$, and $\widetilde{k}$ may be obtained by $\widetilde{\omega}$ based on the linear wave dispersion relation. The above equation is derived for unidirectional waves. In the numerical implementation, the horizontal fluid velocity at Γ_O below the free surface is predicted by $u_h(t)$, and the corresponding vertical fluid velocity satisfies $\frac{\partial u_v}{\partial n} = 0$, where u_v is the vertical fluid velocity at Γ_O. The fluid velocity at Γ_O above the free surface is imposed by a zero-gradient condition. This technique does not need the additional computational domain and has shown promising effectiveness by Yan et al. (2020).

At the inlet boundary Γ_C, the NS solver is coupled with the QALE-FEM, yielding a hybrid model qaleFOAM (Gong et al., 2020; Li et al., 2018; Yan et al., 2020) using the one-way coupling strategy. The primary benefit of using the hybrid model instead of a standalone NS solver is the reduction in computational cost. Further details and its effectiveness are discussed in our previous publications and related studies in the literature, e.g., Paulsen et al. (2014) and Aliyar et al. (2022). In the one-way qaleFOAM, the incident

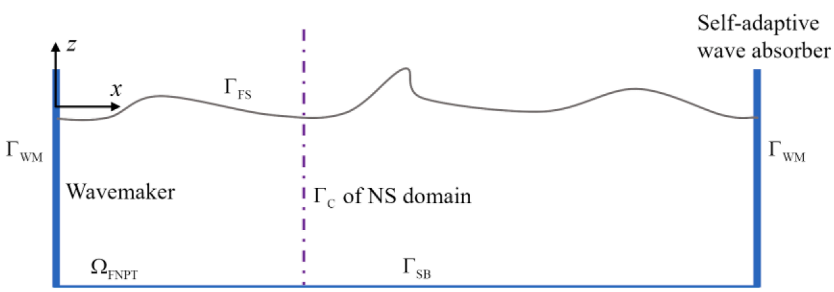

Fig. 2. Illustration of the numerical wave tank adopted by the QALE-FEM (the dot-dashed line corresponding to Γ_C in the NS domain illustrated in Fig. 1).

wave is generated using the QALE-FEM in a separated wave tank sketched in Fig. 2.

This domain is referred to as the FNPT domain ($\Omega_{\rm FNPT}$), that is bounded by an upstream position away from the bodies ($\Gamma_{\rm WM}$), where a wavemaker is employed to generate waves, a flat seabed $\Gamma_{\rm SB}$, the free surface $\Gamma_{\rm FS}$ and the right end boundary $\Gamma_{\rm WM}$. In this study, we adopt the second-order wavemaker theory (Schäffer, 1996) at the left end of $\Omega_{\rm FNPT}$ and utilize a self-adaptive wave absorber developed by Yan et al. (2016) at the right end of $\Omega_{\rm FNPT}$ to minimize the wave reflection. In $\Omega_{\rm FNPT}$, the fluid motion is solved by the potential theory with a velocity potential $\phi(x,y,z,t)$ satisfying Laplace's equation:

$$\nabla^2\phi = 0 \tag{9}$$

On $\Gamma_{\rm FS}$, the kinematic and dynamic conditions are written in the Lagrangian form as:

$$\frac{\mathrm{D}\mathbf{r}}{\mathrm{D}t} = \nabla\phi \tag{10}$$

$$\frac{\mathrm{D}\phi}{\mathrm{D}t} = -g\eta_F + \frac{1}{2}\nabla\phi\cdot\nabla\phi \tag{11}$$

where $\mathbf{r} = (x,y,z)$ is the position vector of a fluid particle on $\Gamma_{\rm FS}$, g is the gravitational acceleration, and η_F is the free surface elevation in the FNPT domain. $\mathrm{D}/\mathrm{D}t = \partial/\partial t + \mathbf{u}\cdot\nabla$ denotes the material derivative, with $\mathbf{u}$ being the velocity of the fluid particle. On other rigid boundaries, $\Gamma_{\rm WM}$ and $\Gamma_{\rm SB}$, the boundary condition is given as:

$$\frac{\partial\phi}{\partial n} = U_n = \mathbf{U}\cdot\mathbf{n} \tag{12}$$

in which $\mathbf{U}$ and $\mathbf{n}$ denote the velocity and unit normal vector of the boundary. In this study, the normal velocity of the boundary U_n is specified on the wavemaker $\Gamma_{\rm WM}$, and $U_n = 0$ on the seabed $\Gamma_{\rm SB}$. The boundary value problem described by Eqs. (9–12) is solved by the QALE-FEM. For more detailed introductions about the numerical implementation of the QALE-FEM, the reader can be referred to Ma and Yan (2006). The high robustness and accuracy of the QALE-FEM in modelling nonlinear waves up to wave breaking have been demonstrated in Yan and Ma (2010a), which guarantees an accurate description of the wave kinematics and reduces the computational cost compared to the NS model.

As all other one-way hybrid models, the results in the NS domain will not feed back into the simulation of the FNPT domain. At each time step, the wave elevation and fluid velocity at $\Gamma_{\rm C}$ will be duplicated and fed to the NS solver as the corresponding boudnary conditions. In the existing qaleFOAM, the fluid velocity at $\Gamma_{\rm C}$ is specified by the solution of the QALE-FEM simulation, i.e.,

$$\mathbf{u}(x,y,z) = \begin{cases} \nabla\phi(x,y,z), z \le \eta_F \\ (1-R_z)\nabla\phi(x,y,\eta_F) + R_z\mathbf{u}_a(x,y,z), z > \eta_F \end{cases} \tag{13}$$

in which R_z is a ramp function from 0 to 1 (see Yan et al., 2020), $\mathbf{u}_a(x,y,z)$ is the air velocity above the free surface and usually set to 0, and the free surface elevation is specified as that obtained by using the QALE-FEM, i.e., η_F. The volume fraction at $\Gamma_{\rm C}$ can then be specified by the ratio of the corresponding wetted area to the total area of the boundary face once η_F at $\Gamma_{\rm C}$ is known. For a detailed description, the reader is referred to Yan and Ma (2010b) and Jacobsen et al. (2012). Clearly, assigning the FNPT solutions to $\Gamma_{\rm C}$ cannot account for the reflected waves from the floating bodies. Consequently, such waves will be re-reflected towards the floating bodies from $\Gamma_{\rm C}$. To avoid this, a relaxation or transition zone is usually required and placed near $\Gamma_{\rm C}$. The solution of the NS model, i.e., Eqs. (1–3), needs to be corrected in the transition zone by a weighted average of the NS solutions and the corresponding FNPT solutions. In this work, the concept of the improved wave absorber (Eqs. (6–8)) used at $\Gamma_{\rm O}$ will be extended to deal with the reflected waves at $\Gamma_{\rm C}$. To do so, the instantaneous wave elevation recorded at $\Gamma_{\rm C}$ is decomposed into two parts, i.e., the incident wave elevation $\eta_F(t)$ specified by the QALE-FEM and the rest $\widehat{\eta}(t)$.

$$\eta(t) = \eta_F(t) + \widehat{\eta}(t) \tag{14}$$

The fluid velocity at time t is also decomposed into two parts, one arising from the incident wave $\mathbf{u}_F$ and the remaining part $\widehat{\boldsymbol{u}}$. The former is specified by $\nabla\phi(x,y,\zeta_1)$, where $\zeta_1 = \frac{z-\eta}{\eta+h}(\eta_F + h) + \eta_F$, and (x, y) is the coordinate of $\Gamma_{\rm C}$ in the FNPT domain. Eq. (8) is extended to specify the horizontal component of $\widehat{\boldsymbol{u}}$. If the incident wave direction is perpendicular to $\Gamma_{\rm C}$, the horizontal fluid velocity below the free surface can be expressed as:

$$u_h(t) = u_{Fh}(t) - \widetilde{\omega}(t)\frac{\cosh(\widetilde{k}(z' + h))}{\sinh(\widetilde{k}h)}\widehat{\eta}(t) \tag{15}$$

in which u_{Fh} is the horizontal component of $\mathbf{u}_F$, $z' = \frac{z-\eta}{\eta+h}h$, and $\widetilde{\omega}$ and $\widetilde{k}$ are obtained using $\widehat{\eta}(t)$ by the same method adopted by Eq. (8). The vertical velocity $u_v(t)$ is specified by the summation of the vertical component of $\mathbf{u}_F$ and the rest part obtained by implementing $\frac{\partial\widehat{u}_v}{\partial n} = 0$, in which $\widehat{u}_v$ is the vertical component of $\widehat{\boldsymbol{u}}$. It is noted that Eq. (8) and Eq. (15) have some theoretical limitations. The first one is the linear or quasi-linear assumptions discussed above, and the second one is due to the assumption that the wave direction is perpendicular to the boundaries. However, the floating bodies in three-dimensional cases may scatter the wave into different directions even though the incident wave is unidirectional. These limitations may result in error. In order to minimise such error, one may need to equip a transition zone, which is expected to be much smaller than that used in the existing one-way coupling approach. For the cases presented in this paper, no transition zone is adopted.

2.2. Motion equations of floating bodies

After solving the governing equations in Ω_{NS}, the hydrodynamic forces and moments on floating bodies can be evaluated by integrating the pressure and viscous stress over the instantaneous body surface. Together with the restraint forces and moments arising from the external mechanical system as well as the gravitational force, the resultant forces and moments on the bodies can be obtained. Then we can apply Newton's second law and Euler's equation to solve the translational and rotational motions of the bodies.

In this work, instead of using the generic motion solver in OpenFOAM, the rotational motion of a rigid body is described in body-fixed coordinates (i.e., $O_b x_b y_b z_b$, as shown in Fig. 1, in which the origin O_b is located at body's centre of gravity) by Euler angles. Following Ma and Yan (2009) and Yan et al. (2020), the motion equation of each body is written as:

$$[\mathbf{M}]\dot{\mathbf{U}}_{\mathrm{c}} = \mathbf{F}_{\mathrm{h}} + \mathbf{F}_{\mathrm{m}} - mg\mathbf{k} \tag{16}$$

$$[\mathbf{I}]\dot{\Omega} + \boldsymbol{\Omega} \times [\mathbf{I}]\boldsymbol{\Omega} = \mathbf{N}_{\mathrm{h}} + \mathbf{N}_{\mathrm{m}} \tag{17}$$

$$\frac{\mathrm{d}\mathbf{X}}{\mathrm{d}t} = \mathbf{U}_{\mathrm{c}} \tag{18}$$

$$[\mathbf{B}]\frac{\mathrm{d}\boldsymbol{\theta}}{\mathrm{d}t} = \boldsymbol{\Omega} \tag{19}$$

where $[\mathbf{M}]$ and $[\mathbf{I}]$ are the mass and moment of inertia matrices; $\mathbf{U}_{\mathrm{c}}$ and $\boldsymbol{\Omega}$ are the translational and angular velocities; $\dot{\mathbf{U}}_{\mathrm{c}}$ and $\dot{\Omega}$ are the translational and angular accelerations; $\mathbf{X} = (\xi_1, \xi_2, \xi_3)$ is the translational displacement and $\boldsymbol{\theta} = (\alpha, \beta, \gamma) = (\xi_4, \xi_5, \xi_6)$ is the Euler angle; $[\mathbf{B}]$ is a transformation matrix defined as:

$$[\mathbf{B}] = \begin{bmatrix} \cos\beta\cos\gamma & \sin\gamma & 0 \\ -\cos\beta\sin\gamma & \cos\gamma & 0 \\ \sin\beta & 0 & 1 \end{bmatrix} \tag{20}$$

In Eqs. (16) and (17), $\mathbf{F}_{\mathrm{h}}$ and $\mathbf{N}_{\mathrm{h}}$ denote the hydrodynamic forces and moments on the body respectively; $-mg\mathbf{k}$ denotes the gravitational force; $\mathbf{F}_{\mathrm{m}}$ and $\mathbf{N}_{\mathrm{m}}$ denote the restraint forces and moments arising from the external mechanical system. In this study, the mechanical system is simplified as a linear pre-tensioned spring together with a linear PTO damper, as shown in Fig. 3. Thus, the restraint force can be written as:

$$\mathbf{F}_{\mathrm{m}} = -(T_0 + k_{\mathrm{s}}\Delta l + B_{\mathrm{PTO}}\Delta\dot{l})\frac{\boldsymbol{l}_{AB}}{|\boldsymbol{l}_{AB}|} \tag{21}$$

where T_0 is the static pre-tension for counteracting the net buoyancy of the body when the body is at rest; k_{s} is the spring stiffness and B_{PTO} is the PTO damping coefficient; Δl and $\Delta\dot{l}$ denote the tether extension and its rate of change with time, respectively. $\boldsymbol{l}_{AB}$ represents

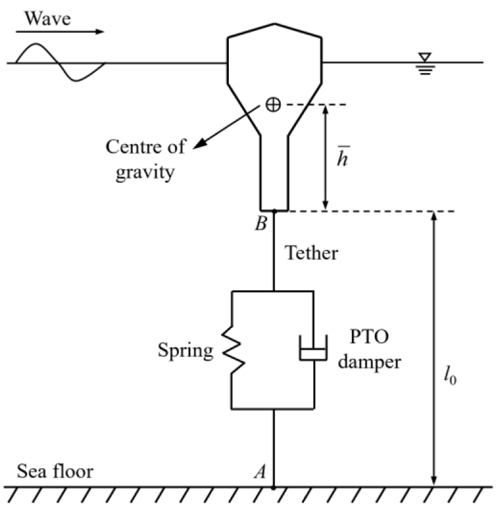

Fig. 3. Definition sketch of the single-tethered buoy and its mechanical system.

the time-varying vector from the anchor point (***A***) on the seabed to the tether attachment point (***B***).

Following Orszaghova et al. (2019) and Zhang et al. (2021), the expression for the tether extension can be derived by including all the translational motions (ξ_1, ξ_2, ξ_3) and rotational motions (ξ_4, ξ_5, ξ_6) of the buoy. In this study, the incident waves and the buoy are symmetric about the *x-z* plane. Thus, only 3-DOF motions are dominant (i.e., surge, heave and pitch), and the expression of Δl can be written as:

$$\Delta l = \sqrt{(\xi_1 - \overline{h}\sin\xi_5)^2 + [\xi_3 + l_0 + \overline{h}(1 - \cos\xi_5)]^2} - l_0 \tag{22}$$

where $\overline{h}$ denotes the distance between the centre of gravity of the buoy and the attachment point, and l_0 denotes the initial length of the tether when the buoy is at rest. The expression of $\Delta\dot{l}$ can be obtained by taking the derivative of Eq. (22) with regard to time, i.e.,

$$\Delta\dot{l} = \frac{(\xi_1 - \overline{h}\sin\xi_5)(\dot{\xi}_1 - \overline{h}\dot{\xi}_5\cos\xi_5) + [\xi_3 + l_0 + \overline{h}(1 - \cos\xi_5)](\dot{\xi}_3 + \overline{h}\dot{\xi}_5\sin\xi_5)}{\sqrt{(\xi_1 - \overline{h}\sin\xi_5)^2 + [\xi_3 + l_0 + \overline{h}(1 - \cos\xi_5)]^2}} \tag{23}$$

The moment arising from the restraint force is given as:

$$\mathbf{N}_\mathrm{m} = \mathbf{r}_\mathrm{m} \times \mathbf{F}_\mathrm{m} \tag{24}$$

in which $\mathbf{r}_\mathrm{m}$ represents the position vector from the centre of gravity of the buoy to the attachment point.

2.3. Dynamic mesh methods

In order to accommodate moving bodies in numerical simulations, the computational mesh needs to change over time according to the movement of the body. Several dynamic mesh motion methods have been available so far, like re-meshing, mesh morphing, sliding mesh interface and overset mesh (Windt et al., 2018, 2020). For WEC simulations, the mesh morphing method is most commonly used among them because of its simplicity, generality and high computational efficiency, as mentioned in Windt et al. (2020). However, for large-amplitude motions, in particular in the cases with multiple floating bodies, the numerical instability may occur and the simulation may crash ultimately as a result of the poor quality of distorted meshes, such as the highly skewed, non-orthogonal cells and/or the cells with large aspect ratios. The overset mesh method theoretically provides a framework for tackling the arbitrarily large body motion within the computational domain, since the mesh quality remains constant throughout the simulation. This is recently attracting increased attention (e.g., Chen et al., 2019; Windt et al., 2020), due to its robust capability of dealing with large-amplitude body motions. However, it gives rise to a substantial increase in computing time and the possible conservation issues due to the interpolation between the overset mesh (body-fitted mesh) and the static background mesh, as found in Chandar (2019).

In the present preliminary study, the mesh morphing method is adopted together with additional treatment to minimise mesh deformation, particularly in the vicinity of the buoys. For cases involving multiple moving bodies, a zone of appropriate size is assigned to each body, with no overlap between adjacent zones. The dynamic mesh motion associated with each body is only within its corresponding zone. Within each zone, the spherical linear interpolation (SLERP) algorithm is employed to determine the displacement of grid points according to their distance from the body surface. For this purpose, the mesh morphing region is specified by two parameters of the inner and outer distance ($\mathrm{d_i}$ and $\mathrm{d_o}$). The grid point follows the motion of the body rigidly in the region within $\mathrm{d_i}$, and it keeps static in the region outside $\mathrm{d_o}$. In the region between $\mathrm{d_i}$ and $\mathrm{d_o}$, the displacement $\delta\boldsymbol{p}_j$ of a grid point whose position vector $\boldsymbol{p}_j$ is defined relative to the centre of rotation is expressed as:

$$\delta\boldsymbol{p}_j = s\mathbf{X} + q_s\boldsymbol{p}_j{q_s}^* - q_0\boldsymbol{p}_j{q_0}^* \tag{25}$$

$$q_s = \left(qq_0^{-1}\right)^s q_0 \tag{26}$$

where s denotes a scale function at the point; $\mathbf{X}$ is the translational displacement of the body, as defined in Eq. (18); q denotes the instantaneous orientation of body, which is expressed in quaternion; q_0 denotes the initial orientation of body; ${q_s}^*$ represents the quaternion conjugate of q_s. The piecewise linear scale function is generally adopted and written as:

$$s = \begin{cases} 1, \mathrm{d} \le \mathrm{d_i} \\ 1 - \dfrac{\mathrm{d} - \mathrm{d_i}}{\mathrm{d_o} - \mathrm{d_i}}, \mathrm{d_i} < \mathrm{d} < \mathrm{d_o} \\ 0, \mathrm{d} \ge \mathrm{d_o} \end{cases} \tag{27}$$

where d represents the minimum distance of a grid point to the body surface. In this study, we also tested several other types of scale functions, i.e., the cosine-type, sine-type and hybrid functions, which are written as respectively:

$$s' = \frac{1 - \cos\pi s}{2} \tag{28a}$$

$$s'' = \sin\frac{\pi}{2}s \tag{28b}$$

$$s''' = (\sin\pi s)s + (1 - \sin\pi s)s' \tag{28c}$$

in which s is given by Eq. (27). Fig. 4 shows the above scale functions with regard to the non-dimensional distance d/d_o.

After comparing the performance of mesh morphing with different scale functions, it was found that the cosine-type scale function provides a smoother transition between different regions, but is more likely to cause compressive deformation in the middle of the mesh morphing region (see in Appendix A). This can be attributed to the larger gradient of the cosine-type scale function than that of the linear one at around $d/d_o = 0.5$, as shown in Fig. 4. Similarly, the sine-type scale function tends to cause significant compressive deformation near the outer boundary of the mesh morphing region. By contrast, the hybrid scale function combines the advantage of both the linear and cosine-type scale functions, maintaining a relatively uniform and small gradient across the mesh-morphing region while still providing a smooth transition between regions, as shown in Fig. A1. It is therefore adopted in the present study.

2.4. Performance evaluation of WECs

As sketched in Fig. 3, the wave energy is extracted from the wave-induced motions of the floating buoy by a PTO system. Following the analysis of Orszaghova et al. (2019) for a similar single-tether buoy based on the linearised approximation, the wave energy is mainly extracted from the buoy's heave motion, as other motion modes are only weakly coupled to the PTO system. Thus, in literature (e.g., Devolder et al., 2017; Jin et al., 2018; Yu and Li, 2013), it is usually assumed that only the heave motion is used to extract the wave power. However, the present model considers the contribution of the buoy's 3-DOF or even 6-DOF motions to the absorbed wave power, and thus the effects of multi-mode coupled motions on the power performance of WECs are incorporated.

The PTO force arising from the PTO damper is defined as:

$$F_{\mathrm{PTO}} = B_{\mathrm{PTO}}\Delta\dot{l} \tag{29}$$

in which the expression of $\Delta\dot{l}$ has been given in Eq. (23). Then the instantaneous absorbed power of the WEC is given as:

$$P_{\mathrm{abs}} = F_{\mathrm{PTO}}\Delta\dot{l} = B_{\mathrm{PTO}}|\Delta\dot{l}|^2 \tag{30}$$

The mean absorbed power of the WEC during the time nT can be written as:

$$\overline{P}_{\mathrm{abs}} = \frac{1}{nT}\int_t^{t+nT} B_{\mathrm{PTO}}|\Delta\dot{l}|^2 dt \tag{31}$$

in which T denotes the wave period.

In order to evaluate the effects of the interaction between WECs in the array on the overall power extraction performance, the q-factor is usually used in studies of WEC arrays (e.g., Child and Venugopal, 2010; Wolgamot et al., 2012). Normally, the q-factor is defined as the ratio of the maximum absorbed power by the array of WECs to that by the same number of isolated WECs, assuming that the optimal operating conditions can be satisfied. Nevertheless, due to the motion constraints of the WECs and the limits of the mechanical system in practical scenarios, the optimal operating conditions for the WECs cannot be satisfied for all wave conditions. Moreover, it is difficult to accurately determine the optimal conditions if various nonlinear factors are considered. So in this study, a modified non-optimal q-factor is defined as:

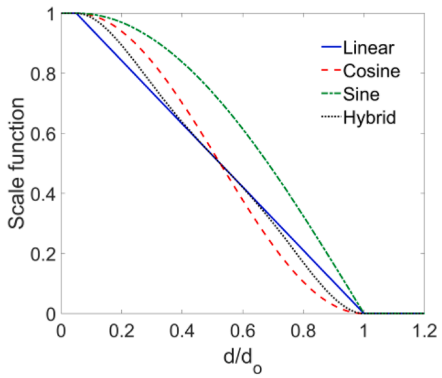

Fig. 4. Various scale functions for the mesh morphing with $d_i/d_o = 0.05$.

$$q = \frac{\sum_{j=1}^{N_B} P_j}{N_B P_0} \tag{32}$$

where N_B is the number of buoys in the array, P_j denotes the mean absorbed power by the jth buoy, and P_0 denotes the mean absorbed power by a single isolated buoy under the same wave condition. The values of P_0 and P_j ($j = 1, \ldots, N_B$) can be calculated by Eq. (31). It should be noted that the q-factor defined in Eq. (32) is a non-optimal q-factor evaluated under the prescribed PTO damping and mechanical constraints. The present definition is intended to quantify the relative influence of array interactions under a fixed and practically constrained operating condition.

3. Numerical setup and validation study

3.1. WEC model: CorPower buoy

In this paper, we consider the wave energy device developed by the CorPower Ocean company. The device has been tested at a model scale of 1:16 in the wave tank at Ecole Centrale de Nantes in France. The geometry and dimensions of the CorPower buoy model are sketched in Fig. 5. In the experiments, a rope was used to connect the buoy to a motor rig. The rope attached to the buoy was pre-tensioned and the motor rig was utilized to approximately simulate the PTO system. The details of the experimental set-up were given in Todalshaug et al. (2016). The key parameters are summarized in Table 2. Note that a simplified mechanical device consisting of a linear pre-tensioned spring and a linear PTO damper as sketched in Fig. 3 is used in numerical simulations. The water depth of 5.0 m used in the validation case follows the original experimental setup, where the depth was not scaled from the prototype design water depth due to experimental constraints. This setting is retained here to allow direct comparison with the measured data.

3.2. Numerical settings

This section introduces the numerical settings briefly, including the size of the computational domain, the numerical schemes for temporal and spatial discretizations, and the solution and algorithm control.

3.2.1. Computational domain

As shown in Fig. 2, the left end of Ω_{FNPT} equips a piston or flap wavemaker to generate the incident waves at the upstream of the buoy, and a self-adaptive wave absorber is adopted at the right end of Ω_{FNPT} to prevent the wave reflection from the boundary. The length of Ω_{FNPT} is set to 60 m, which is usually in the range of $6\lambda \sim 8\lambda$, where λ denotes the incident wavelength. The initial height of Ω_{FNPT} is the same as the water depth and then varies with the movement of the free surface. For the computational mesh in Ω_{FNPT}, the size of the horizonal grid is about $\lambda/100$ and the number of vertical layers is set to 20 based on the preliminary convergence tests.

The NS domain (Ω_{NS}) is solely confined around the buoys, and the distance from the axis of the front/rear buoy to the inlet/outlet boundary and side walls of the NS domain is set to 2.0 m based on the numerical tests, which is about 4 times the diameter of the buoy. It is noted that no relaxation zone is contained near the inlet or outlet boundary in this study due to the use of the improved self-adaptive coupling approach as introduced in Section 2.1, which leads to a significant decrease of the computational cost for a smaller computational domain. The computational mesh in Ω_{NS} used here is generated with a built-in meshing utility snappyHexMesh

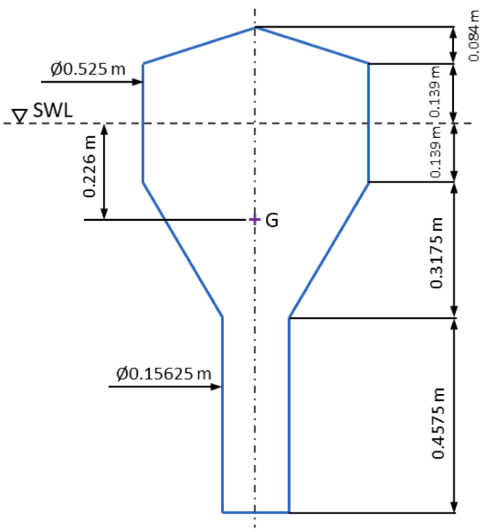

Fig. 5. Geometry and dimensions of the CorPower buoy.

Table 2
Experimental set-up.

Parameter	Value
Buoy diameter	0.525 m
Mass of buoy	19.1 kg
Moment of inertia	2.34 kg·m^2
Vertical centre of gravity	−0.226 m
Water depth	5.0 m
Depth at mooring point	3.09 m
Mooring line spring stiffness	202 N/m
Pre-tension force	500 N

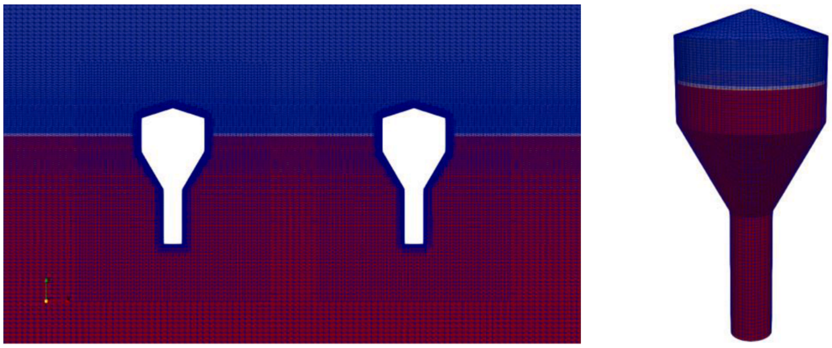

(a) (b)

Fig. 6. Sketch of the computational mesh for two CorPower buoys (red: water; blue: air), (a) The computational mesh in longitudinal section in fluid domain; (b) Mesh on the buoy.

Table 3
Parameters of different computational meshes.

Mesh scheme	Base Δx	Base Δy	Base Δz	Number of cells (million)
Mesh 1	$\lambda/52$	$\lambda/39$	$H/10.0$	0.118
Mesh 2	$\lambda/78$	$\lambda/78$	$H/13.3$	0.425
Mesh 3	$\lambda/117$	$\lambda/97.5$	$H/20.0$	1.015
Mesh 4	$\lambda/156$	$\lambda/97.5$	$H/26.7$	1.672
Mesh 5	$\lambda/156$	$\lambda/117$	$H/33.3$	2.402

of OpenFOAM. For instance, Fig. 6(a) shows the sketch of the computational mesh in the longitudinal section (i.e., x–z plane) for the wave interaction with two CorPower buoys with a distance of 2.0 m. Three regions of the computational mesh can be specified as: (i) the background mesh region, (ii) the region near the free surface, (iii) the region around each of the floating buoys. The background mesh is hierarchically refined in regions (ii) and (iii) to make sure an adequate grid resolution around the free surface and the buoys. In addition, the background mesh beyond the refined free surface region is stretched in the z-direction with an expansion ratio of 3.

3.2.2. Solver and algorithm

In this paper, the two-phase RANS-VOF solver interDyMFoam is used in the NS domain as mentioned before. The PIMPLE algorithm is utilized to solve the velocity–pressure coupling, which combines the PISO algorithm with the SIMPLE algorithm. The standard finite volume discretization scheme is used here for divergence, gradient and diffusion terms together with various interpolation schemes, which are used for interpolations of values from cell centres to cell faces. For time integration, a blended first-order Euler/second-order Crank–Nicolson scheme is adopted in this study. The maximum Courant number is set to 0.5, with an initial time step of 0.005 s. During the simulations, the time step is automatically adjusted to satisfy the Courant–Friedrichs–Lewy (CFL) condition. For the FNPT solver QALE-FEM, a constant time step of $T/150$ is adopted. To address the difference in time-step sizes between the two solvers, a second-order polynomial interpolation method (Yan and Ma, 2010b) is used to feed the QALE-FEM data to interDyMFoam at the required time instants.

3.3. Mesh and time-step convergence

It is well known that the accuracy of the CFD results is mainly dependent on the spatial and temporal discretization levels. In order to assess the error of spatial discretization, the mesh convergence study is carried out, and the temporal discretization is controlled by

Table 4
Numerical results using different computational meshes.

	Mesh 1	Mesh 2	Mesh 3	Mesh 4	Mesh 5
Surge (m)	0.4184	0.4277	0.4352	0.4409	0.4429
Heave (m)	0.0933	0.0955	0.0969	0.0973	0.0975
Pitch (deg)	7.516	7.875	8.086	8.198	8.239
Mean absorbed power (W)	30.259	30.423	30.691	30.852	30.829

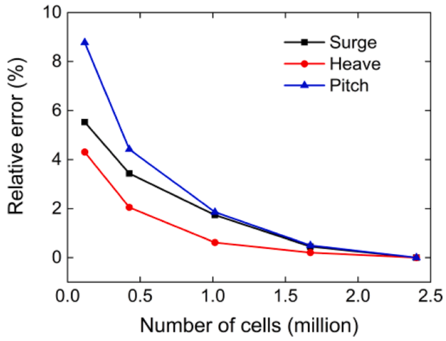

Fig. 7. Relative error of results using different computational meshes.

the maximum Courant number. In this section, the case of regular wave interaction with two CorPower buoys is presented with the wave period $T = 2.25$ s and wave height $H = 0.40$ m as an example. Five spatial discretization levels have been examined, and the basic parameters of the five computational meshes with different grid resolutions and cell numbers are listed in Table 3. The base Δx, Δy, Δz denote the grid size for the background mesh along the x-, y- and z-directions, respectively.

Table 4 presents the motion responses and mean absorbed power of the front buoy (i.e., Buoy 1) using different computational meshes. The listed values are the average motion amplitudes and mean absorbed power over 10 wave periods when the simulation reaches the steady state. The relative errors with respect to the finest-mesh results are shown in Fig. 7. The results obtained using Mesh 4 are nearly converged, with relative errors below 1% for all three motion responses compared with the finest-mesh results. The average absorbed power is even less sensitive to mesh refinement, with smaller relative errors among the different meshes. Similar mesh-convergence behaviour is also observed for the rear buoy. Therefore, the discretisation level of Mesh 4 is adopted in the following simulations.

In the temporal sensitivity check, the results obtained with the adopted CFL limit were compared with those from a smaller time step/lower maximum Courant number. The comparison shows negligible differences in the main motion responses and power-related quantities, indicating that the selected adaptive time-stepping strategy is sufficient for capturing the main trends discussed in this study.

3.4. Validation tests

In this section, the surge decay test of the CorPower buoy is firstly carried out in calm water to validate the present model. The numerical set-up is the same as the experimental set-up shown in Table 2. To quantify the accuracy of the numerical model, a normalised root-mean-square error (NRMSE) is defined as:

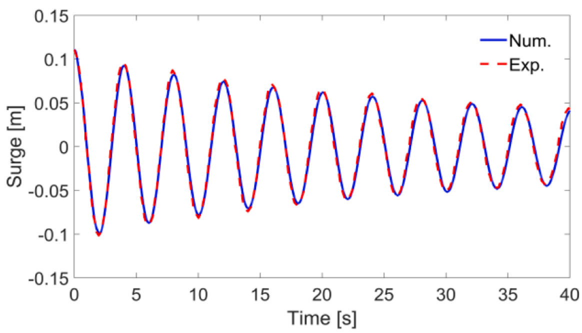

Fig. 8. Surge decay test of the CorPower buoy.

$$\mathrm{NRMSE} = \frac{\sqrt{\frac{1}{N}\sum_{i=1}^{N}\left(f_i^{\mathrm{num}} - f_i^{\mathrm{exp}}\right)^2}}{\max\left(f_i^{\mathrm{exp}}\right)} \tag{33}$$

where superscripts, ‘num’ and ‘exp’, denote the numerical and experimental results respectively, and $\max\left(f_i^{\mathrm{exp}}\right)$ denotes the maximum value of the corresponding experimental data. Fig. 8 shows the numerical results of the surge decay compared with the experimental data, and a quite good agreement is seen with the NRMSE <5%, which implies an accurate prediction of both the natural period and damping ratio in surge mode.

The regular wave interaction with a single CorPower buoy is then simulated and compared to the experimental results (see Wang et al., 2018) for further validation. The incident wave period is 2.25 s, and the wave height is 0.156 m. In this wave condition, the PTO damping coefficient is set to 628 kg/s, which is selected near the optimal value estimated based on the linear hydrodynamics (e.g., Falnes, 2002). It is seen from Fig. 9 that the agreement between the numerical and experimental results is quite reasonable, and the normalised root-mean-square errors (NRMSE) of surge, heave and pitch responses are all <10%. These results provide preliminary support for the capability and accuracy of the present numerical model. However, the present validation is limited by the lack of array-scale experimental data. Further validation against dedicated array experiments is needed in future work. In addition, it appears that the amplitudes and periods of the numerical responses do not significantly change with time after 20 s. This implies that the concept of the improved wave absorbing technique is effective, which provides a satisfactory absorption of the reflected waves at the inlet/outlet boundary of the NS domain and enables long-duration simulations within a limited computational domain without requiring an extended relaxation zone. The performance of the improved wave absorber is further evaluated in Appendix B through comparison with the conventional relaxation-zone implementation for a representative two-buoy case.

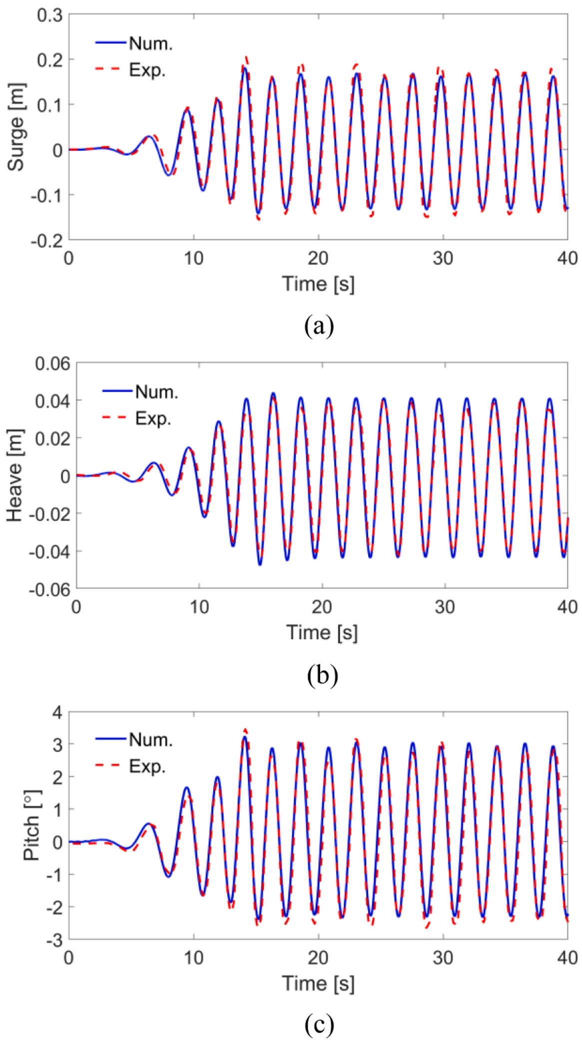

Fig. 9. Comparison of motion responses of the CorPower buoy. (a) Surge; (b) Heave; (c) Pitch.

4. Results and discussion

In this section, the regular wave interaction with two and three CorPower buoys installed in a line array is investigated with various wave conditions to study the effects of nonlinear interactions between waves and multiple floating buoys. All buoys in the array have the same geometry and are equally-spaced. The parameters of each buoy are the same as the model in the above validation case, and the distance (d) between the vertical axes of the two neighbouring buoys is set to 2.0 m, which is about 4 times the diameter of the buoy. In contrast to the validation case, the water depth is reduced to 3.125 m in the following array simulations, corresponding to the design water depth of 50 m at the prototype scale of the buoy. In this study we only consider the cases when the incident wave direction is parallel to the array, i.e., in head waves. In the following simulations, the sizes of the NS domain used for two and three CorPower buoys are 6 m and 8 m long, respectively, 4 m wide and 5.125 m high (i.e., from −3.125 m to 2.0 m), and the spatial discretization level similar to Mesh 4 is adopted based on the mesh convergence tests as shown in Section 3.3.

4.1. Effect of wave steepness

The regular wave cases with the wave period $T = 2.25$ s and wave heights $H = 0.156\sim0.42$ m (i.e., $kR = 0.211$, $d/\lambda \approx 0.256$ and $kA = 0.063\sim0.169$, where k is the wave number; λ is the wave length; R is the radius of the upper cylindrical section of the buoy; and A is the incident wave amplitude represented as half of the wave height) are considered here to investigate the effect of wave steepness kA. The wave period at the buoy's prototype scale is 9.0 s, which is corresponding to a typical operational sea state for the buoy. The PTO damping coefficient B_{PTO} is set to 628 kg/s for each buoy in these cases, which is close to the optimal value for power extraction as mentioned before.

Fig. 10 shows the time series of the normalised surge, heave and pitch responses of two CorPower buoys for $kA = 0.063$ and 0.169. Buoy 1 and Buoy 2 represent the front and rear buoy, respectively. As expected, phase shifts are observed between the responses of the

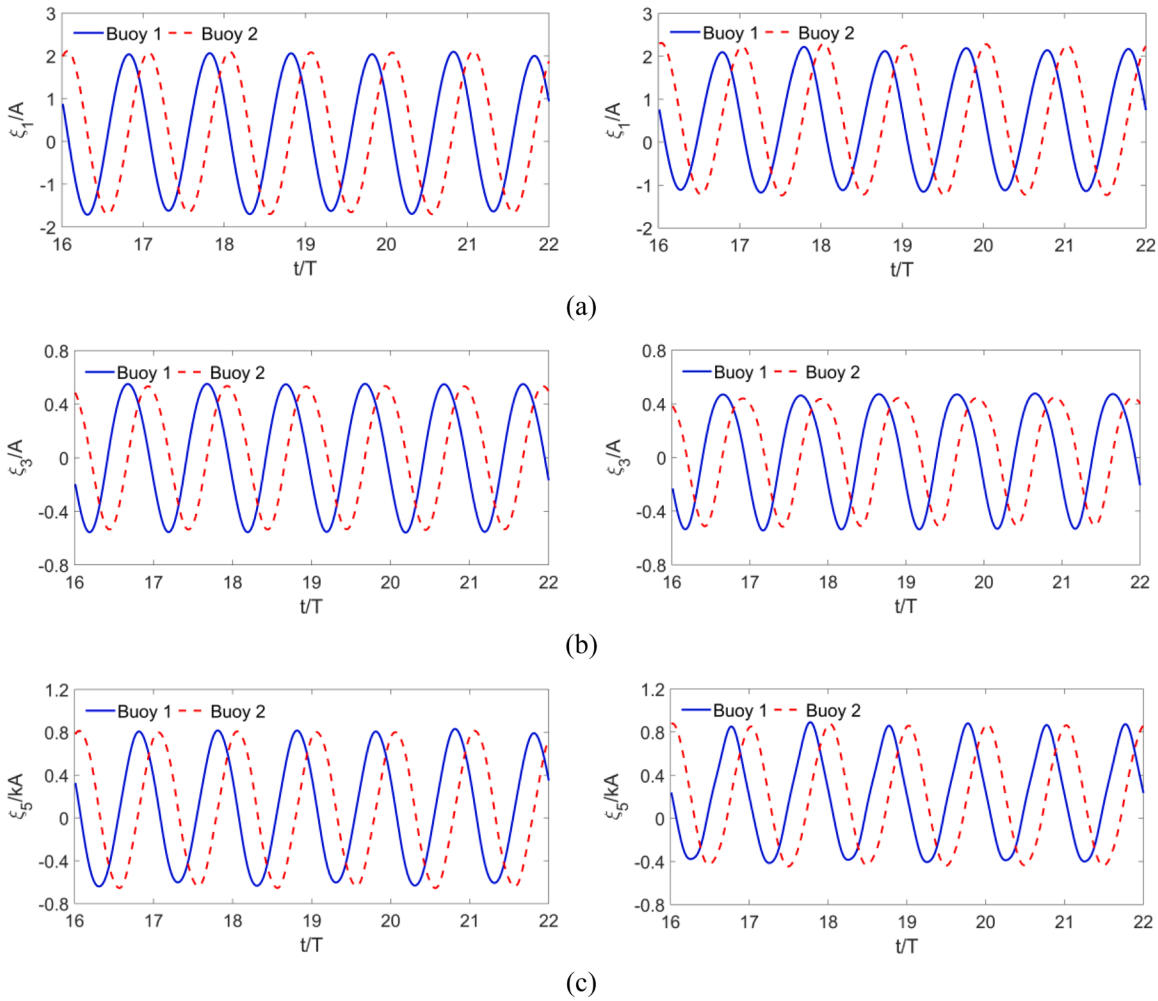

Fig. 10. Time series of motion responses with $kA = 0.063$ (left) and $kA = 0.169$ (right). (a) Surge; (b) Heave; (c) Pitch.

two buoys, whereas the differences in their motion amplitudes are relatively small. This may be related to the relatively large buoy spacing compared with the buoy diameter and the small buoy dimensions compared with the incident wavelength. The hydrodynamic interaction between the two buoys is relatively weak in these cases. Consequently, the observed changes in the normalised surge and pitch responses with increasing kA are mainly interpreted as the effect of incident-wave nonlinearity. In particular, the upward shift of both the peaks and troughs of the normalised surge and pitch responses indicates an increase in the mean drift of both buoys with wave steepness.

To further analyse the influence of nonlinearity on the motion responses, the Fourier analysis over 10 wave periods is then performed to obtain the harmonic components when the simulation has reached the steady state. Fig. 11 and Fig. 12 present the normalised amplitudes (indicated by superscript 'amp') of the harmonic components of the motion responses against the wave steepness for Buoy 1 and Buoy 2, respectively. The surge and pitch responses are mainly composed of the first-harmonic component and the mean drift while the contributions of the second-harmonic component are negligible. The normalised first-harmonic amplitudes of the surge and pitch responses decrease with increasing kA. In contrast, their normalised mean drifts increase with increasing kA almost linearly. Since the motion responses have been normalised by A or kA, the approximately linear variation here indicates that the actual mean drifts scale approximately with A^2 or equivalently with $(kA)^2$ for the fixed wave period considered here. For the heave motions, the first-harmonic amplitude is much more dominate compared to the second-harmonic amplitude and the mean drift. The present analysis is restricted to regular waves and therefore focuses on the influence of wave steepness on harmonic responses and mean drift. Future work may extend the simulations to bichromatic waves or narrow-banded irregular waves, in which wave-component interactions can generate difference-frequency loads. These low-frequency loads may contribute to slow-drift surge and pitch motions and may also affect low-frequency hydrodynamic interactions within WEC arrays. Such extensions would provide further insight into the nonlinear array response under more realistic sea states.

Fig. 13 shows the mean absorbed power of each buoy calculated by Eq. (31) corresponding to different wave steepness, in which the steady-state data lasting 10 wave periods were used. The normalised mean absorbed power keeps nearly constant with increasing kA, and the mean power absorbed by Buoy 2 is slightly less than that absorbed by Buoy 1. However, the time series of the normalised instantaneous absorbed power strongly depends on the wave steepness, as shown in Fig. 14. The occurrence of two absorbed-power peaks within each wave period can be understood from the definition of the absorbed power. Since the instantaneous absorbed power is proportional to the square of the tether-extension rate, as given in Eq. (30), both the extension and contraction phases of the tether can generate positive power peaks. Within each wave period, the two dominant local maxima of the absorbed power are identified. As illustrated in Fig. 15, the larger of these two maxima is defined as the higher peak P_H, while the smaller one is defined as the lower peak

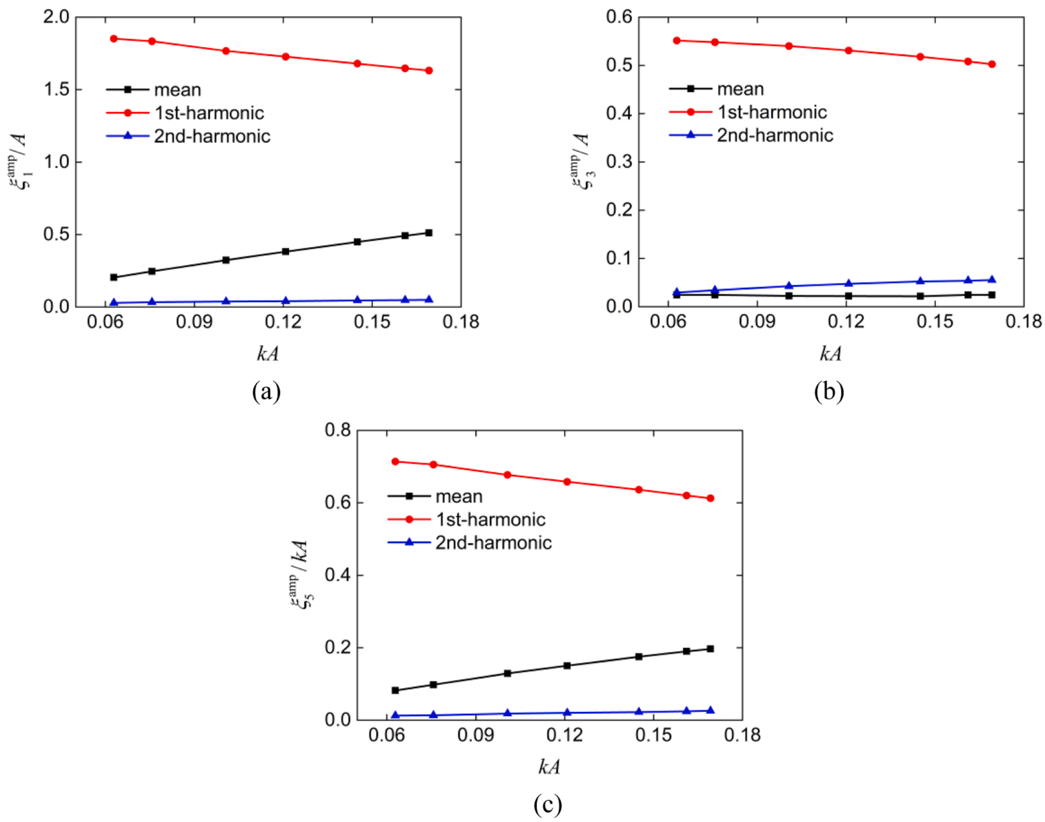

Fig. 11. Harmonic components of motion responses for Buoy 1 with different wave steepness. (a) Surge; (b) Heave; (c) Pitch.

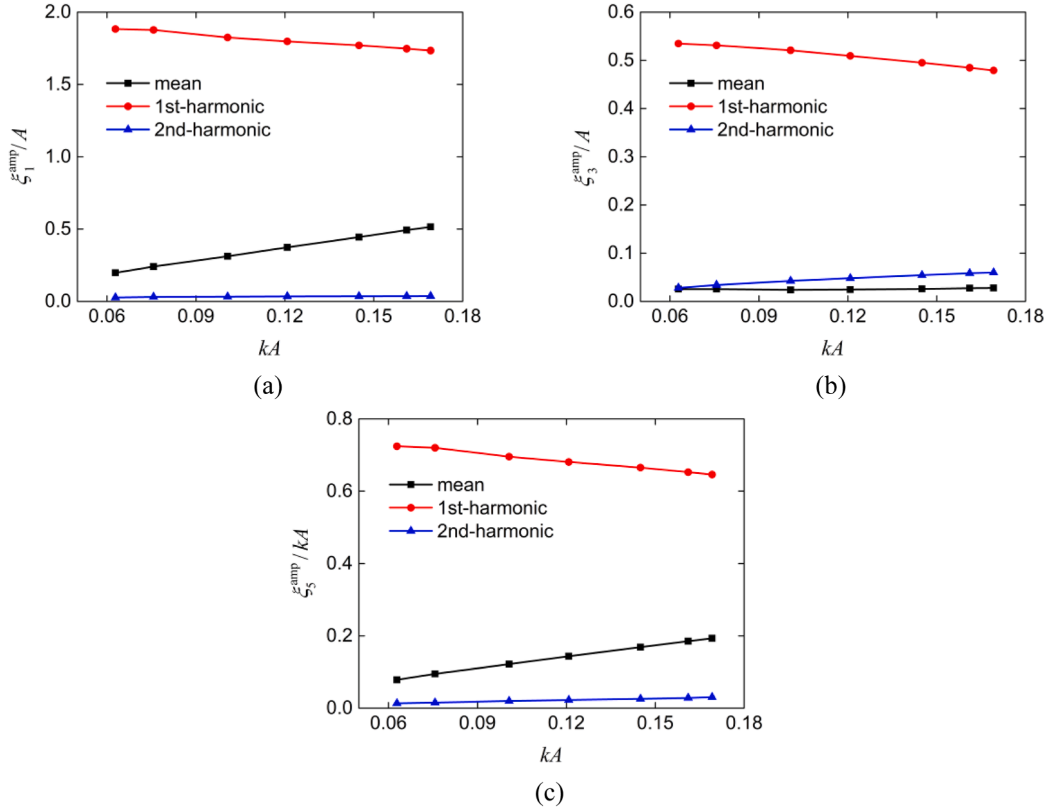

Fig. 12. Harmonic components of motion responses for Buoy 2 with different wave steepness. (a) Surge; (b) Heave; (c) Pitch.

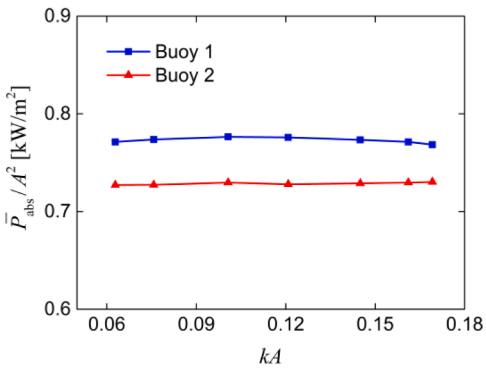

Fig. 13. Mean absorbed power of each buoy with different wave steepness.

P_L. The corresponding duration times t_H and t_L are determined from the time intervals associated with the two adjacent power-peak branches. Fig. 16 shows the peak-power ratio P_H/P_L and the duration-time ratio t_H/t_L against different wave steepness, which are obtained by averaging the corresponding values over the selected steady-state wave periods. Theoretically, both these ratios should be equal to 1.0 if the waves and induced motions are all linear. However, with the increase of nonlinearity, the power ratio P_H/P_L for the two buoys increases dramatically. This may be attributed to the nonlinear dependence of the tether-extension rate $\Delta\dot{l}$ on the coupled surge, heave and pitch motions and their velocities, as indicated by Eq. (23), rather than on the heave motion alone. As the wave steepness increases, the nonlinear coupling and phase relations among these motion components may change, making the two half-cycles of $\Delta\dot{l}$ increasingly asymmetric. The power ratio for the largest wave steepness is about twice of that for the lowest wave steepness considered here. Apart from this, the power ratio for Buoy 2 is significantly larger than that of Buoy 1. On the other hand, the duration time ratio t_H/t_L decreases gradually as kA increases, indicating that the high peak of the power becomes narrower and the low peak becomes wider. The above findings suggest that the control strategy may need to consider the nonlinear effects.

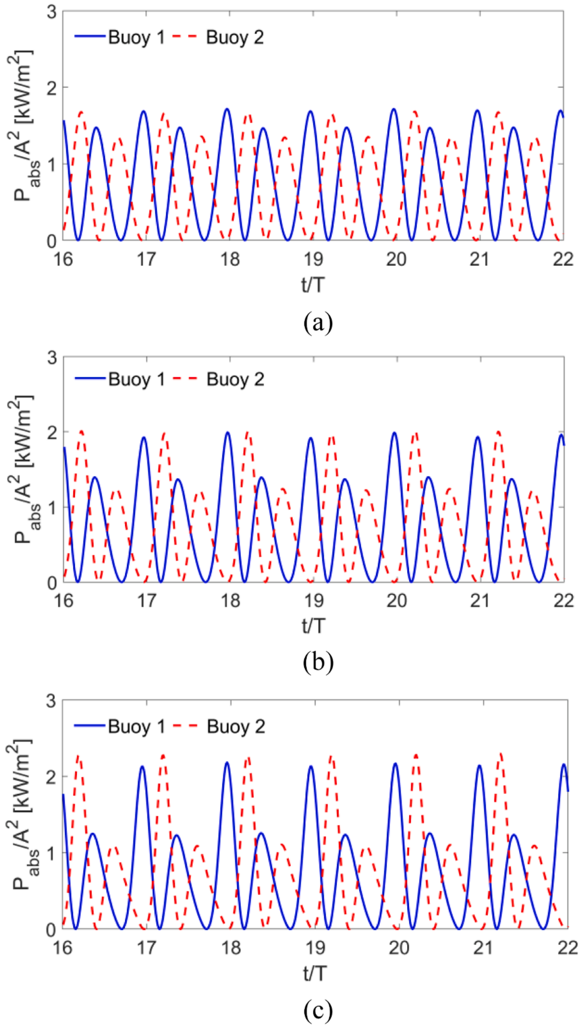

Fig. 14. Time series of the normalised instantaneous absorbed power. (a) $kA = 0.063$; (b) $kA = 0.121$; (c) $kA = 0.169$.

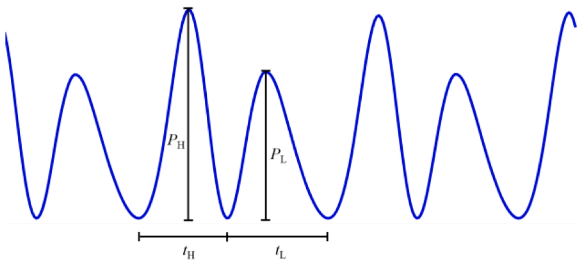

Fig. 15. Definition sketch of the peak power (P_H, P_L) and duration time (t_H, t_L).

4.2. Effects of PTO damping on overtopping

One of nonlinear effects is wave overtopping over the buoys, which cannot be handled by the linear hydrodynamic model. In the present study, overtopping is identified based on the instantaneous free-surface field near the buoy top. Overtopping is considered to occur when the instantaneous free surface rises above the top edge of the upper cylindrical section of the buoy and water enters the conical upper section. Overtopping may be affected by several factors, one of which is the PTO damping. In this subsection, the influences of PTO damping coefficients (B_{PTO}) on wave overtopping and the power extraction performance of the CorPower buoy are investigated. A series of B_{PTO} ranging from 127 to 1802 kg/s is considered under a regular wave condition with a wave period $T = 2.25$

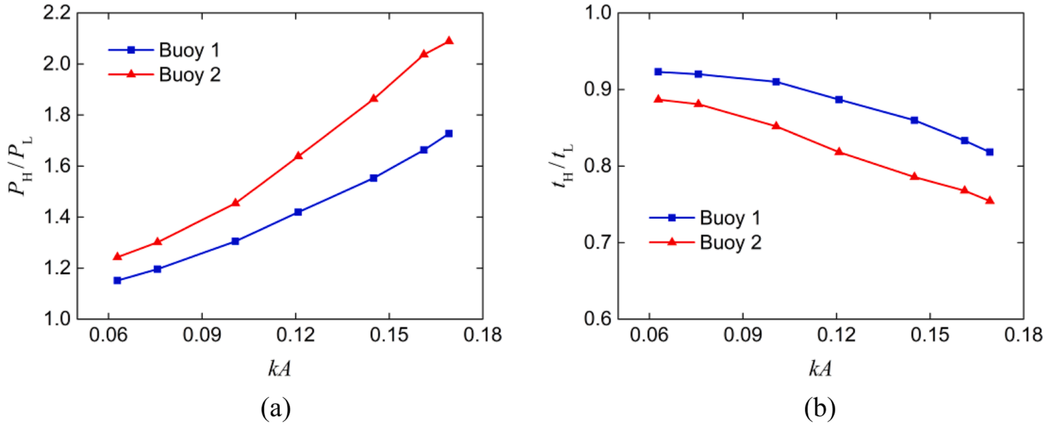

Fig. 16. Peak power and duration time ratios with different wave steepness under T = 2.25 s and B_{PTO} = 628 kg/s. (a) Peak power ratio; (b) Duration time ratio.

s and a wave height $H = 0.42$ m. Other parameters remain the same as those in Section 4.1.

Fig. 17 and Fig. 18 show the snapshots of the longitudinal section through the geometrical centre of the two CorPower buoys for four values of PTO damping coefficients at $t/T = 7.56$ and 7.82, respectively. The first instant corresponds to a wave crest passing Buoy 1, while the second instant corresponds to the same wave crest passing Buoy 2. Based on these illustrations and others we check but do not present, we find that water can significantly overtop the buoys when the PTO damping coefficient is larger than 628 kg/s, such as $B_{PTO} = 1020$ and 1802 kg/s, while no or little overtopping occurs when the PTO damping coefficient is at or smaller than this value for the cases considered. The present analysis focuses on the occurrence of overtopping under different B_{PTO}, while a more detailed quantitative evaluation of overtopping duration and overtopping volume will be considered in future work. The overtopping becomes more significant with increasing B_{PTO}, as shown in Fig. 17(c) and (d) and Fig. 18(c) and (d). This is consistent with the expectation that a larger PTO damping coefficient may increase the restraint force on the buoys, thereby constraining their motions relative to the

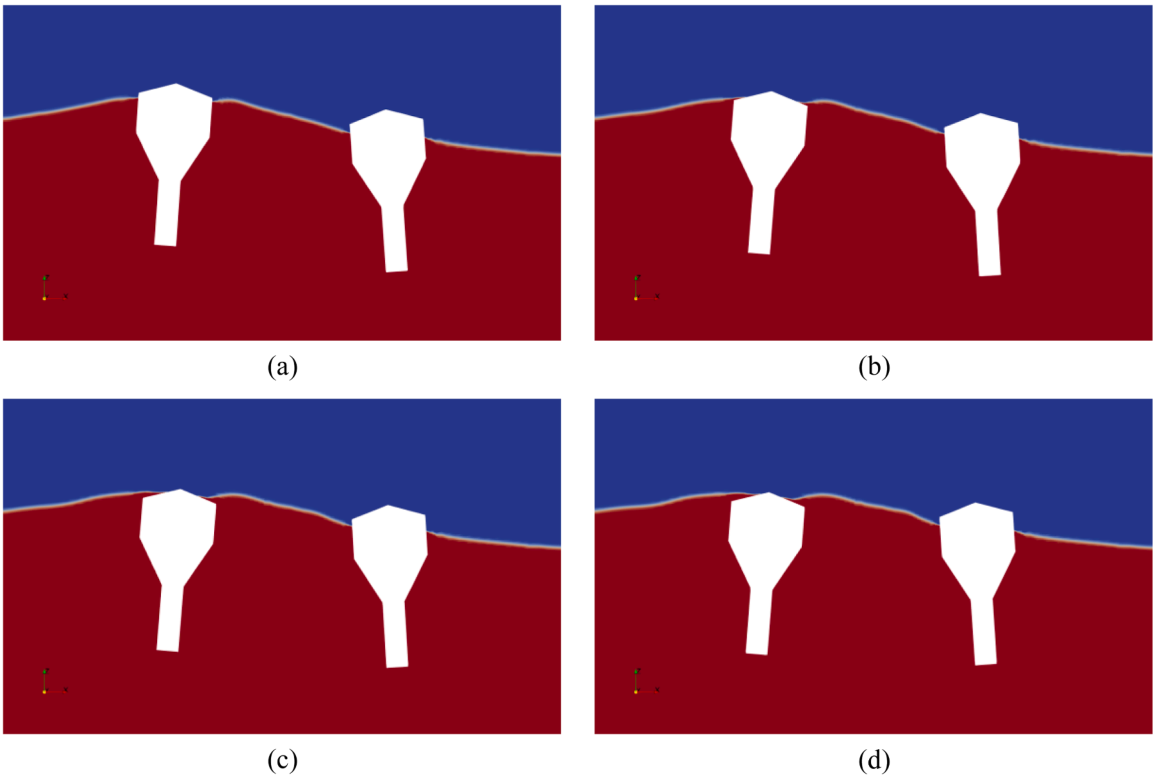

Fig. 17. Snapshots of longitudinal section at $t/T = 7.56$ with different PTO damping coefficients under $T = 2.25$ s and $H = 0.42$ m (red: water; blue: air). (a) B_{PTO} = 238 kg/s; (b) B_{PTO} = 628 kg/s; (c) B_{PTO} = 1020 kg/s; (d) B_{PTO} = 1802 kg/s.

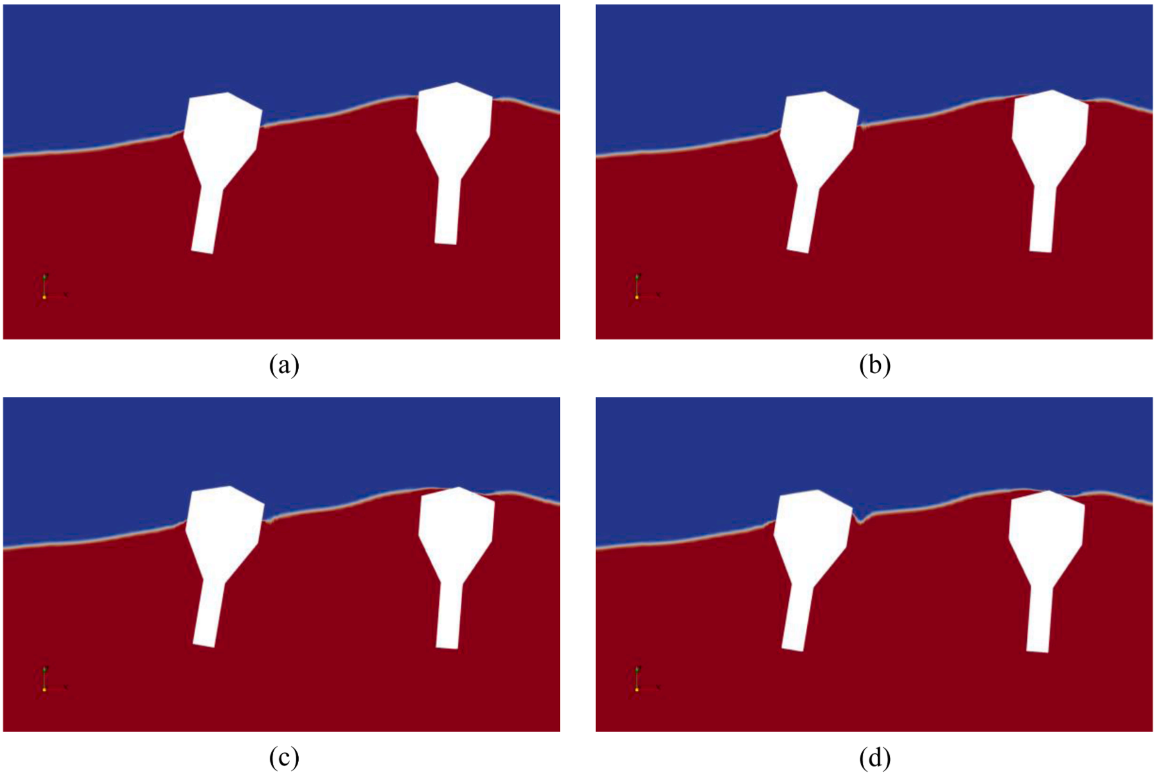

Fig. 18. Snapshots of longitudinal section at $t/T = 7.82$ with different PTO damping coefficients under $T = 2.25$ s and $H = 0.42$ m (red: water; blue: air). (a) $B_{\text{PTO}} = 238$ kg/s; (b) $B_{\text{PTO}} = 628$ kg/s; (c) $B_{\text{PTO}} = 1020$ kg/s; (d) $B_{\text{PTO}} = 1802$ kg/s.

waves. This is further illustrated in Fig. 19 and Fig. 20, which show the normalised heave responses and restraint forces acting on the two buoys, respectively. Comparing Fig. 19 and Fig. 20, the heave response and restraint force are largely in phase, while their amplitudes vary oppositely with PTO damping: a larger heave amplitude generally corresponds to a smaller restraint force, and vice versa. Table 5 and Table 6 list the tether-force statistics for the two buoys under different B_{PTO}. The results show that increasing B_{PTO} mainly increases the maximum and RMS tether forces, while the mean force remains almost unchanged. This indicates that larger PTO damping primarily enhances the tether-force fluctuations and transient peak loads. Fig. 21 further shows the phase shift between the buoy heave response and the corresponding incident wave at the buoy axis, which generally increases with increasing PTO damping. This may enhance the relative motion between the buoys and the surrounding free surface, thereby contributing to the occurrence of overtopping.

Further, the effect of PTO damping coefficients on the power extraction performance of the buoys is evaluated under the same wave condition. Fig. 22 shows the mean absorbed power of each buoy with various PTO damping coefficients. For the convenience of discussions, the heave RAO and normalised PTO force amplitude are also shown in this figure. In the figure, the PTO damping coefficient B_{PTO} is normalised by its nominal optimal value $B_{PTO}^{(\text{opt})}$, which is 628 kg/s for this wave condition. We can see that the heave RAO decreases whereas the PTO force amplitude increases with the increase of B_{PTO}. In other words, an increase of B_{PTO} leads to a reduced buoy velocity but an enlarged PTO force, and hence there should be an optimal B_{PTO} to achieve the maximum power extraction according to Eq. (30). As shown in Fig. 22(c), the mean absorbed power increases firstly and then decreases with B_{PTO}. For the cases we have tested, each buoy has an optimal performance of power extraction when B_{PTO} is at its nominal optimal value, i.e., $B_{PTO}/B_{PTO}^{(\text{opt})} = 1.0$. It is noted that the mean absorbed power of Buoy 2 is slightly less than that of Buoy 1, which may be related to the shielding effect.

As has been discussed about Fig. 14, there are two different peaks in each wave period in the time histories of the absorbed power, and their difference depends on the wave steepness. It is interesting to examine how the change of PTO damping coefficients affects the time histories of the absorbed power as well as the peak differences. For this purpose, Fig. 23 depicts a part of time histories of the absorbed power of the two buoys corresponding to four different PTO damping coefficients, while Fig. 24 shows the corresponding ratio of the power peaks. It is observed that the power ratio increases rapidly with increasing PTO damping coefficients when $B_{\text{PTO}} \leq 628$ kg/s, where no significant overtopping is observed. For larger B_{PTO}, where overtopping becomes significant, the power ratio still increases but at a considerably reduced rate. Although overtopping cannot be identified as the sole factor responsible for this reduced rate of increase, it may play a contributing role. Further investigations are required to shed more light.

Note that a laminar-flow model is adopted in the present simulations. This is considered appropriate for capturing the global

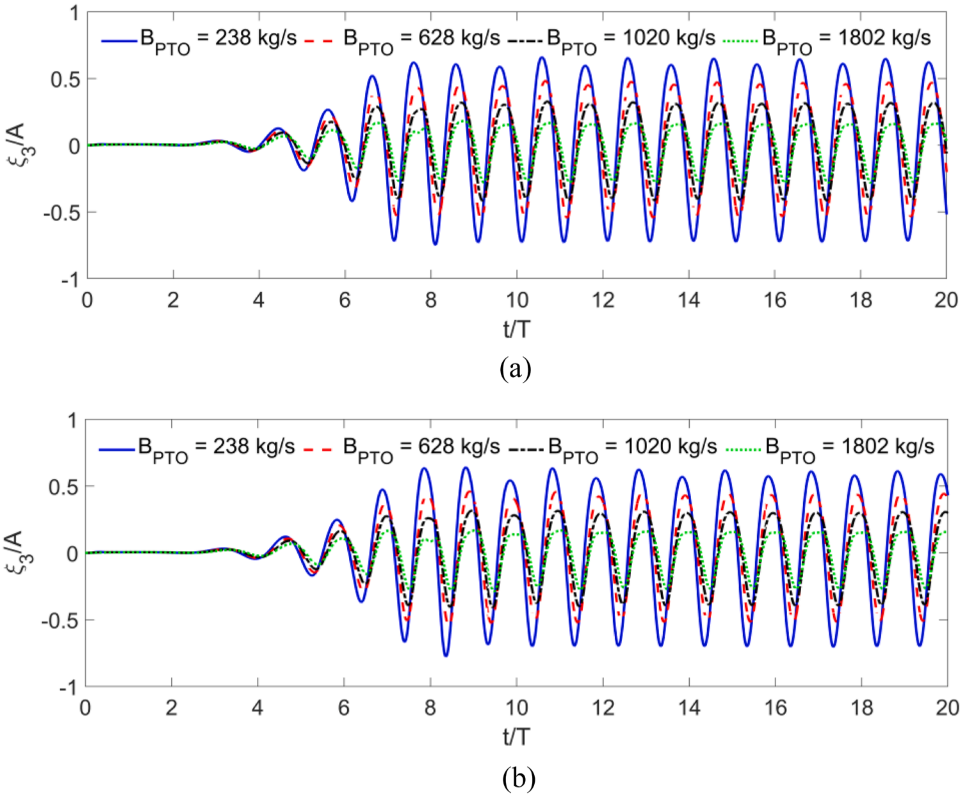

Fig. 19. Time series of heave response for Buoy 1 and 2 with different PTO damping coefficients. (a) Buoy 1; (b) Buoy 2.

response trends, since the buoy motion, absorbed power and tether-force variation are mainly governed by wave inertia, pressure loading, gravity and PTO dynamics. Nevertheless, turbulence may affect detailed overtopping features, such as jet breakup, splash dynamics and overtopping volume. Therefore, the overtopping analysis is interpreted mainly in terms of occurrence and relative significance, rather than as a fully resolved prediction of local turbulent-flow processes.

4.3. Nonlinear buoy interactions in the array

Note that the numerical results presented above are mainly for longer wave scenarios, i.e., the distance between neighbouring buoys is comparatively small relative to the wave length. Under the circumstances, the hydrodynamic interaction between buoys is relatively insignificant, and thus the motion responses and power extraction are similar for each buoy in the line array, as shown in the previous subsections. However, the ocean wave lengths (or periods) vary in a range, and so the hydrodynamic interaction for different wave lengths (or periods) needs attention. For this purpose, this subsection will discuss the cases with various wave periods. To be closer to arrays in practice, three CorPower buoys installed in a line array are considered, each of them being the same as those discussed in the above sections. The wave periods in the range of 1.25 s to 2.75 s (5 s to 11 s in full scale) are considered here and the wave height H is set to 0.30 m except for the shortest wave period for which $H = 0.156$ m is used to avoid incident wave breaking. The spacing distance (d) between two neighbouring buoys is set to 2.0 m, the same as before. This corresponds to the non-dimensional spacing d/λ ranging from 0.18 to 0.82, where λ denotes the incident wavelength and varies from case to case. The PTO damping coefficient B_{PTO} is set to 628 kg/s for each buoy in these cases.

Fig. 25(a) shows the normalised mean absorbed power of each buoy with various non-dimensional spacings. For comparison, the results for a single isolated buoy under the same wave conditions are also presented. Note that the spacing distance (d) is not relevant for the single buoy but it is still used for plotting its results to keep consistency with others. In the figure, Buoys 1, 2 and 3 represent the front, middle and rear buoy, respectively. It appears that the mean absorbed power of Buoy 1 is almost the same as that of the single buoy under the condition of longer waves (i.e., $d/\lambda < 0.4$). Nevertheless, for shorter wave conditions or larger values of d/λ, the mean absorbed power of Buoy 1 can be slightly larger or smaller than that of the single buoy, attributed to the interference of Buoy 2 and 3 on Buoy 1. In addition, mean absorbed powers of Buoy 2 and 3 are significantly smaller than that of the single buoy, and the difference of their powers from that of single buoy is larger than that of Buoy 1 when d/λ is quite large, such as in the range of 0.6∼0.8. This suggests that the buoy interaction has more impact on Buoy 2 and 3 than on Buoy 1 in the range. To shed more light on the buoy interaction, Fig. 25(b) shows the variation of the q-factor calculated by Eq. (32) against the non-dimensional spacing d/λ. The q-factor is <1.0 in the whole range considered in this study, indicating that the interaction between buoys reduces the power absorption of the WEC array.

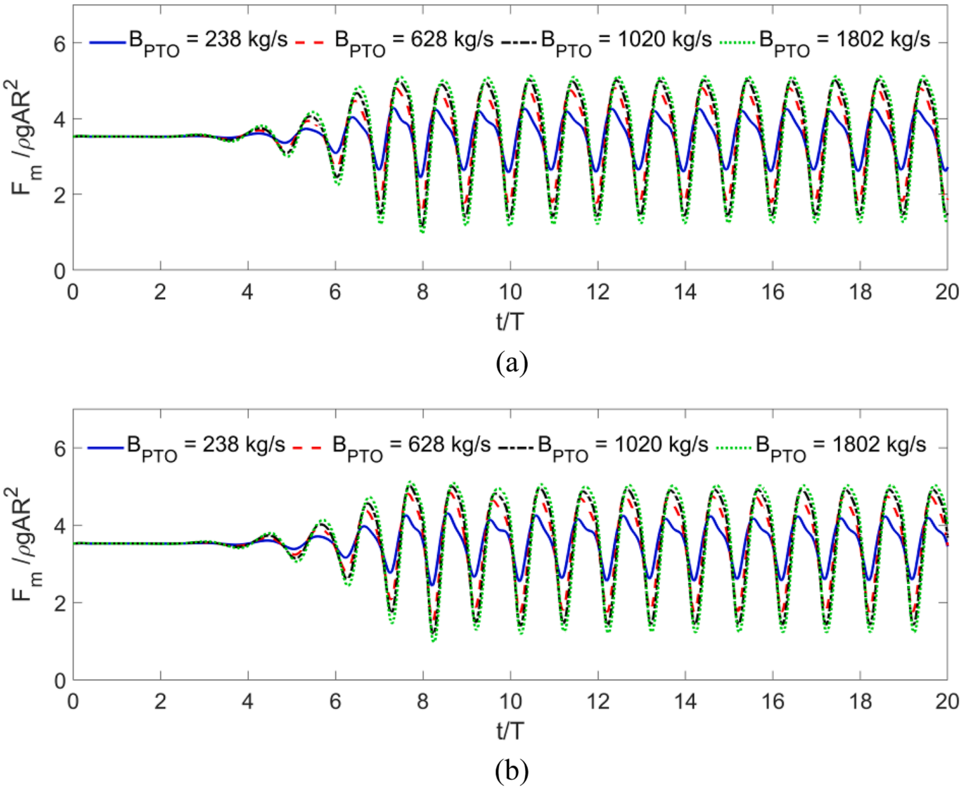

Fig. 20. Time series of restraint force on Buoy 1 and 2 with different PTO damping coefficients. (a) Buoy 1; (b) Buoy 2.

Table 5
Tether-force statistics for Buoy 1 under different PTO damping coefficients (unit: N).

	$B_{PTO} = 238$ kg/s	$B_{PTO} = 628$ kg/s	$B_{PTO} = 1020$ kg/s	$B_{PTO} = 1802$ kg/s
Maximum	605.1693	684.2144	712.8039	728.8302
Mean	503.6045	503.1231	502.4430	501.8631
RMS value	509.1580	524.8182	532.8182	538.5245

Table 6
Tether-force statistics for Buoy 2 under different PTO damping coefficients (unit: N).

	$B_{PTO} = 238$ kg/s	$B_{PTO} = 628$ kg/s	$B_{PTO} = 1020$ kg/s	$B_{PTO} = 1802$ kg/s
Maximum	603.7172	679.2095	703.3316	717.7894
Mean	503.9108	503.4628	503.0201	502.4561
RMS value	509.2848	523.3556	532.0712	538.0195

More specifically, with increasing d/λ, the q-factor gradually increases before it reaches a maximum; then it decreases to reach a minimum at about $d/\lambda = 0.485$; after that it increases again before reaching another but lower maximum; finally it gradually decreases when $d/\lambda > 0.6$. This trend is consistent with some results of Liu et al. (2022) who employed a linear semi-analytical approach combining the interaction theory (Kagemoto and Yue, 1986) with the boundary element method (Liu, 2019) to investigate buoy interactions in a long array. However, because the present q-factor is evaluated under fixed PTO damping and constrained operation, the comparison is mainly qualitative. Fig. 26 depicts the normalised amplitudes of the heave response, vertical hydrodynamic force and dynamic tether force as functions of the non-dimensional spacing d/λ. It is seen that under shorter wave scenarios ($d/\lambda > 0.5$), the amplitudes of heave response and vertical hydrodynamic force for the middle and rear buoys are notably smaller than those for the front buoy. This may be associated with the shielding and phase-interference effects within the array, and is consistent with the variation of absorbed power shown in Fig. 25(a). The dynamic tether force exhibits a similar variation and remains close in magnitude to the vertical hydrodynamic force, indicating a strong coupling between the wave-induced vertical loading and the tether response. Therefore, the nonlinear multi-buoy interaction affects not only the power absorption, but also the tether-load distribution among the devices.

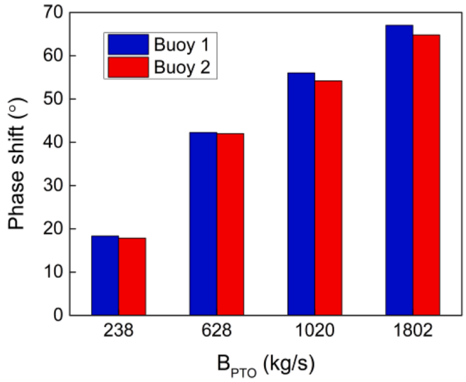

Fig. 21. Phase shift between the heave response of the buoy and the corresponding incident wave elevation.

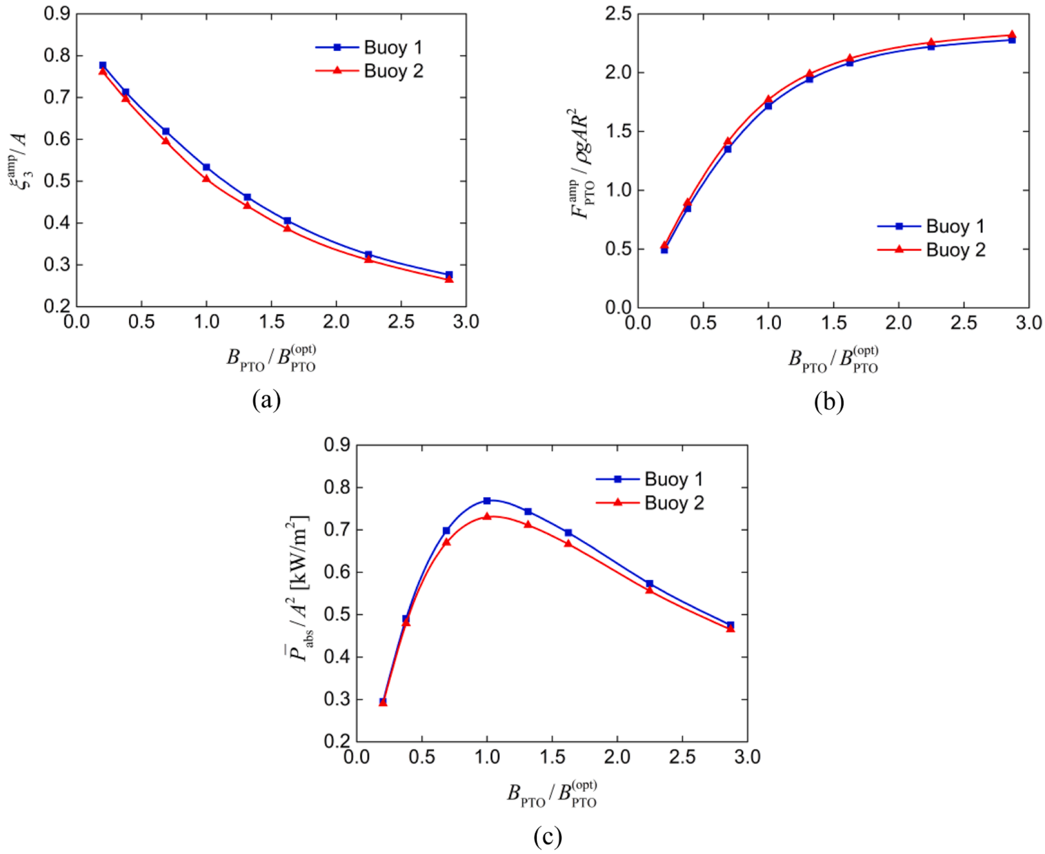

Fig. 22. Motion responses and power extraction performance of the buoy with different PTO damping coefficients. (a). Heave RAO; (b) Normalised PTO force; (c) Mean absorbed power.

A further point of interest is about how the nonlinearity affects the hydrodynamic interaction between buoys. To this end, we further compare the numerical results using various wave heights for two specific wave periods. One is at $d/\lambda = 0.485$, corresponding to the minimum q-factor, and another at $d/\lambda = 0.678$, a typical shorter wave scenario, as seen in Fig. 25(b). Fig. 27 shows the normalised mean absorbed power of each buoy with various wave steepness for these two specific wave periods, and Fig. 28 shows the variation of the corresponding q-factor against the wave steepness. It appears in Fig. 27 that for $d/\lambda = 0.485$, the normalised mean absorbed power of each buoy in the array keeps nearly constant with increasing kA, while it gradually decreases for the single isolated buoy. The interaction between buoys makes the mean absorbed power of each buoy in the array all smaller than that of the single isolated buoy as discussed above. Similar trend for $d/\lambda = 0.678$ is observed but the normalised mean absorbed powers of Buoy 2 and Buoy 3 are smaller than that of the single buoy while Buoy 1 has a larger mean absorbed power being consistent with that in Fig. 25(a).

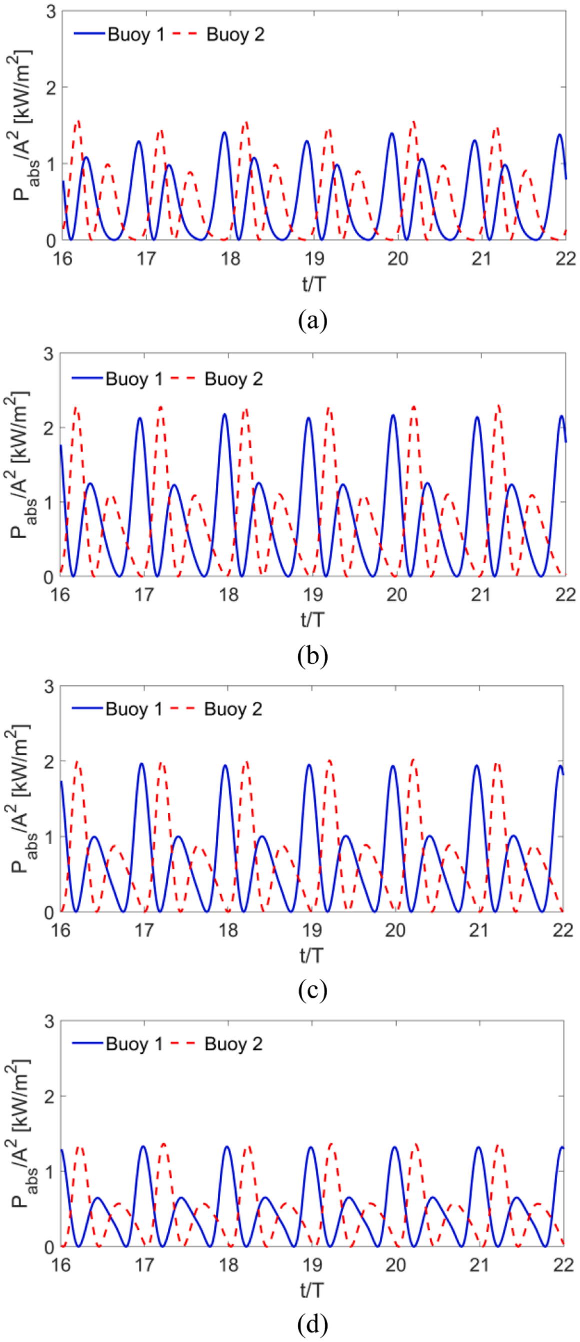

Fig. 23. Time series of the normalised instantaneous absorbed power with different PTO damping coefficients. (a) $B_{\mathrm{PTO}} = 238$ kg/s; (b) $B_{\mathrm{PTO}} = 628$ kg/s; (c) $B_{\mathrm{PTO}} = 1020$ kg/s; (d) $B_{\mathrm{PTO}} = 1802$ kg/s.

From Fig. 28, the q-factor slightly increases and then keeps nearly constant with the increase of wave steepness for both $d/\lambda = 0.485$ and 0.678. In other words, the buoy interaction is slightly weaker in stronger nonlinear waves than in linear waves.

Furthermore, the influence of wave nonlinearity on the detailed power-absorption characteristics is examined. Fig. 29 and Fig. 30 show the peak power and duration time ratios of the adjacent two peaks in the time histories of the absorbed power against different wave steepness for $d/\lambda = 0.485$ and 0.678 respectively. The results of a single isolated buoy are also provided for comparison. Similar to the results in Fig. 16 for two buoys, the power ratios P_H/P_L increase while the duration time ratios t_H/t_L decrease with increasing kA for the three buoys. However, since the values of d/λ here are different, apart from the difference in the number of buoys from that for Fig. 16, their relative variations are different here. More specifically, the power ratios of Buoy 2 for $d/\lambda = 0.485$ in Fig. 30(a) are smaller than those of Buoy 1 at smaller values of kA considered, rather than larger than the later as shown in Fig. 16(a), while the

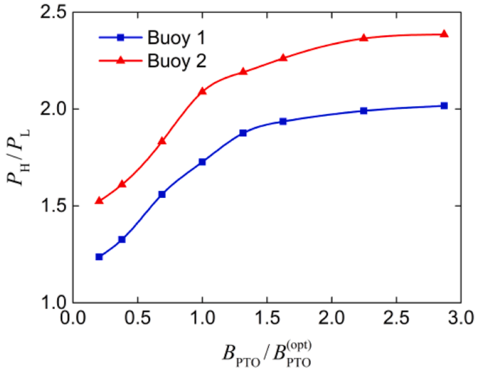

Fig. 24. Peak power ratios with different PTO damping coefficients under $T = 2.25$ s and $H = 0.42$ m.

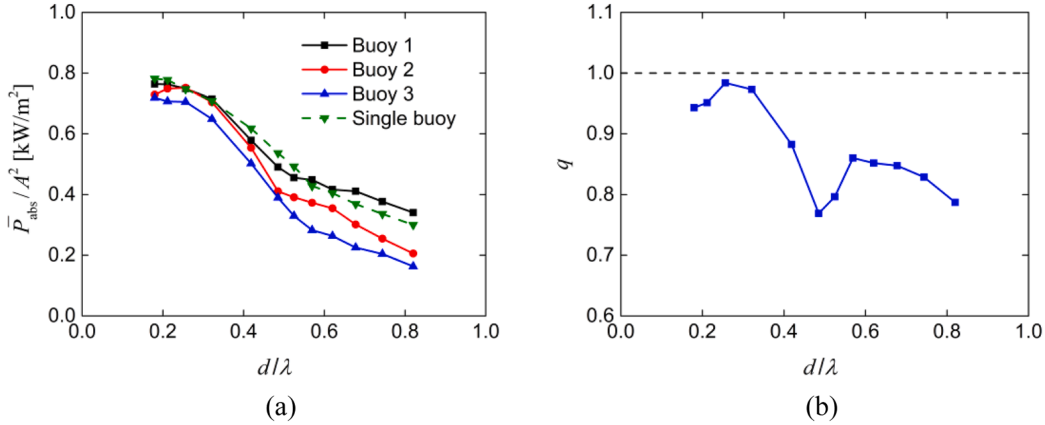

Fig. 25. Power-absorption metrics as functions of the non-dimensional spacing d/λ. (a) Mean absorbed power; (b) q-factor.

duration time ratios are opposite, i.e., higher here but lower in Fig. 16(b) at smaller values of kA. In addition, both ratios of Buoy 2 are largely in between Buoy 1 and Buoy 3 at most values of kA except for the largest one considered. For d/λ= 0.678, the story is slightly different as seen by comparing Fig. 29 with Fig. 30. The power ratios of Buoy 2 are lower than those of Buoy 1 but higher than those of Buoy 3 while the duration time ratios of Buoys 2 and 3 are almost the same but larger than those of Buoy 1 at all values of kA. These results suggest that the variation of these ratios with wave steepness depends on both the number of buoys and the relative spacing d/λ. Nevertheless, the ratios clearly show considerable sensitivity to wave steepness in all cases considered. Clearly more investigations are required for revealing full pictures of behaviours of the ratios in future work.

The above results have practical implications for PTO tuning and array design. The increase in peak-power asymmetry with wave steepness and PTO damping suggests that PTO parameters should not be selected solely based on mean absorbed power, but should also account for nonlinear power fluctuations and possible overtopping risk. In addition, the variation of the q-factor and the differences among individual buoys suggest that array spacing and layout may affect not only the mean power capture of the whole array, but also the distribution of power absorption and dynamic loading among devices. These implications, however, should be interpreted within the restricted scope of the present study, which is limited to head-sea regular wave conditions and prescribed PTO damping settings. Further studies under irregular and directionally spread waves are needed before general design recommendations can be made.

5. Conclusions

In this study, we extend the hybrid model qaleFOAM to study the nonlinear interaction between waves and arrays of point-absorber WECs. It has been demonstrated that the present model can accurately simulate the surge decay and wave-induced motion responses of a single-tethered CorPower buoy through the comparison with the experimental data. On this basis, the nonlinear hydrodynamic interaction with multiple CorPower buoys deployed in a line array is investigated by changing the wave steepness and PTO damping coefficients. In particular, the nonlinear effects on motion responses, absorbed power and the q-factor reflecting the interaction between buoys are examined. The following interesting observations have been made for the cases considered.

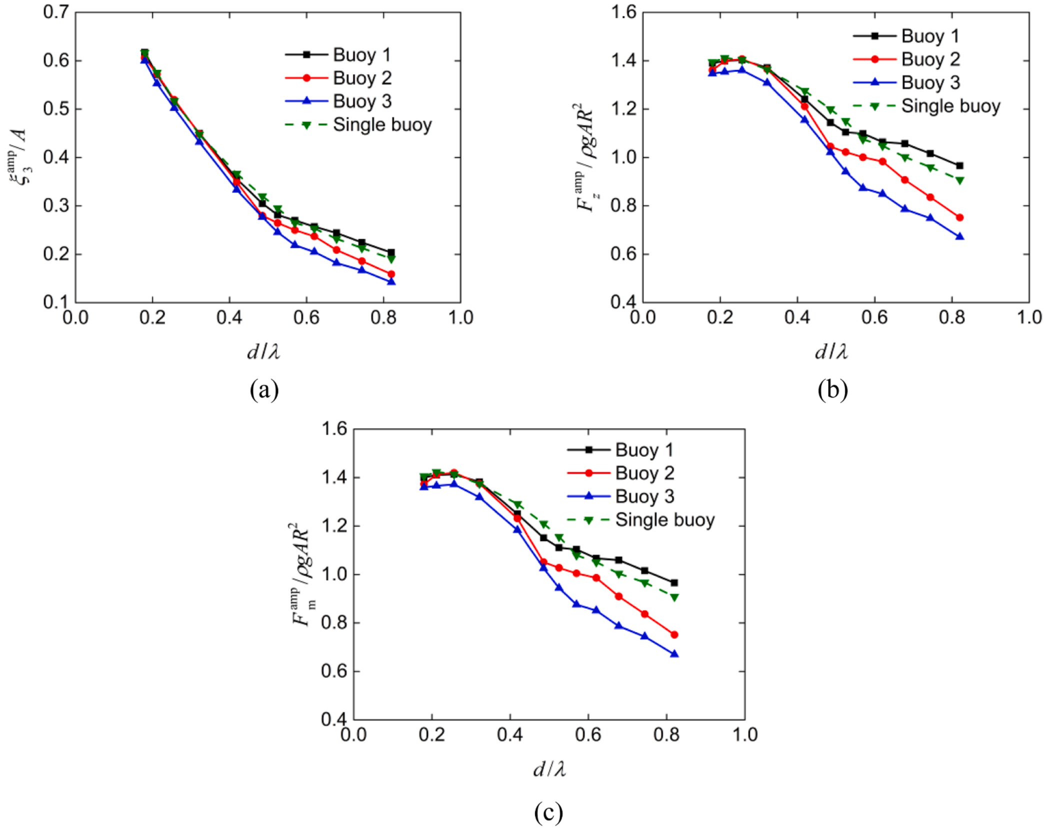

Fig. 26. Normalised heave response and force characteristics as functions of the non-dimensional spacing d/λ. (a) Heave RAO; (b) Vertical hydrodynamic force; (c) Dynamic tether force.

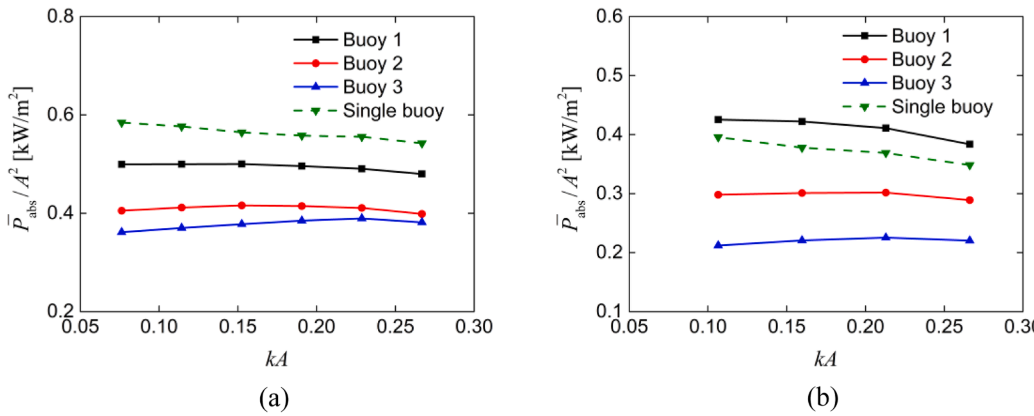

Fig. 27. Mean absorbed power of each buoy with various wave steepness. (a) $d/\lambda = 0.485$; (b) $d/\lambda = 0.678$.

(1). With increasing the wave nonlinearity, the normalised first-harmonic amplitudes linearly decrease but the mean surge and pitch drift linearly increase.
(2). There are two peaks in the time history of the absorbed power in each wave period. The ratios of the larger power peak to smaller one in each wave period significantly increase with the wave nonlinearity becoming stronger. However, the behaviours of the ratios for different buoys depend on the arrangement of buoys and their relative distance. For the arrangement of two buoys with $d/\lambda \approx 0.256$, the ratios of Buoy 2 are larger than those of Buoy 1 for all wave steepness considered. For the arrangement of three buoys with larger values of d/λ, the ratios of Buoy 3 are smaller than Buoy 1 for all wave steepness considered but the ratios of Buoy 2 can be larger than those of Buoy 1 when the nonlinearity becomes strong enough.

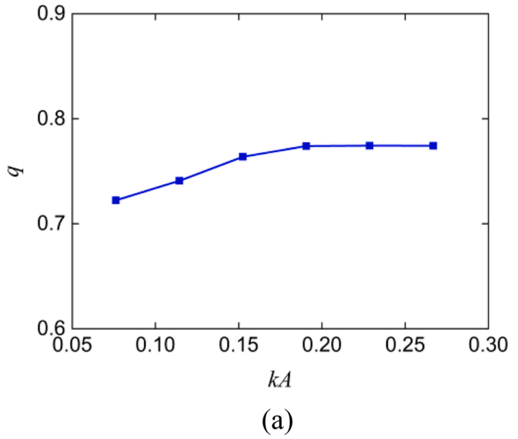

Fig. 28. Variation of the q-factor against the wave steepness. (a) $d/\lambda = 0.485$; (b) $d/\lambda = 0.678$.

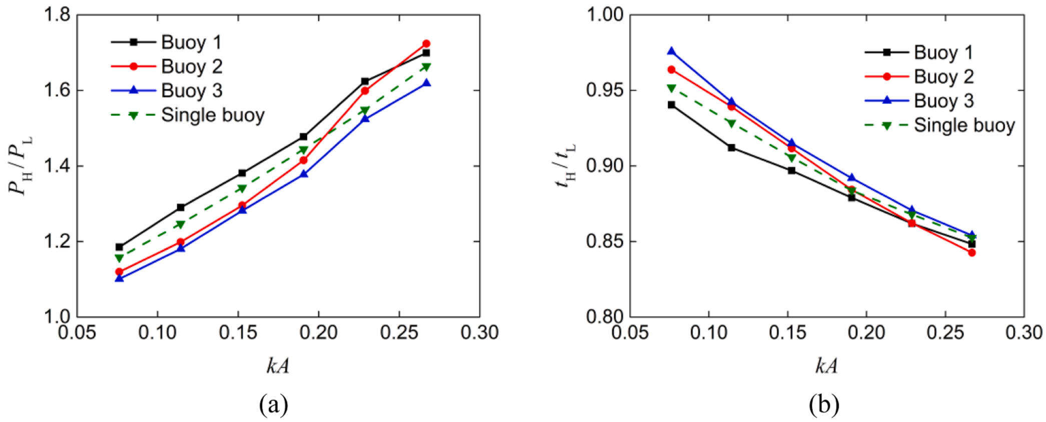

Fig. 29. Peak power and duration time ratios against different wave steepness with $d/\lambda = 0.485$. (a) Peak power ratio; (b) Duration time ratio.

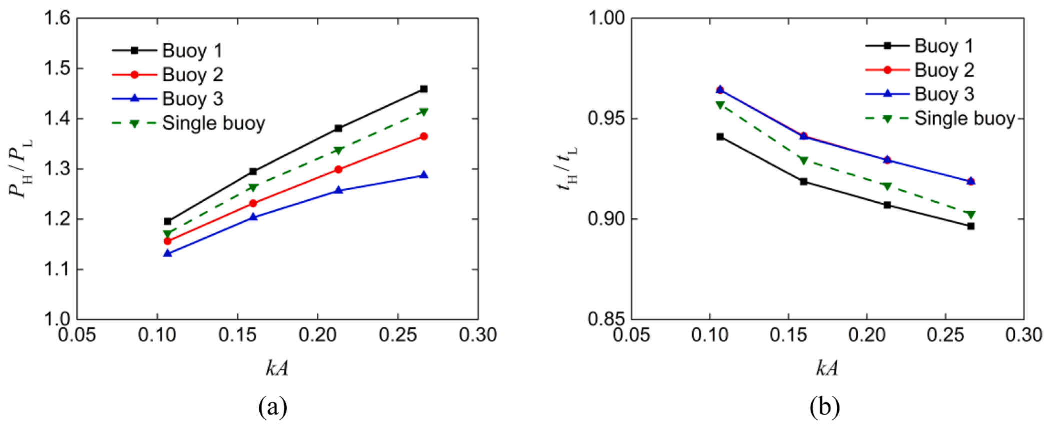

Fig. 30. Peak power and duration time ratios against different wave steepness with $d/\lambda = 0.678$. (a) Peak power ratio; (b) Duration time ratio.

(3). The q-factor reflecting the interaction between buoys slightly increases and then keeps nearly constant with increasing the wave steepness, that is the buoy interaction is slightly weaker with the wave nonlinearity becoming stronger.
(4). When the PTO damping is sufficiently large, wave overtopping on the buoy can occur, which may lead to change in the behaviours of buoys. In particular, the peak power ratios increase rapidly with PTO damping coefficients when no significant overtopping occurs but they increase much slower after significant overtopping has occurred.

The present validation is limited by the lack of array-scale experimental data. Therefore, the array-interaction results should be interpreted as numerical predictions within the present modelling framework rather than as comprehensively validated conclusions. Further validation against dedicated array experiments is needed in future work. Furthermore, it should be emphasised that the present conclusions are drawn from the specific cases considered in this study, which are limited to regular head waves, line-array configurations, a small number of buoys, and prescribed PTO damping settings. Therefore, the observed nonlinear interaction effects and q-factor trends should be interpreted within this tested parameter space. Their applicability to irregular seas, oblique wave incidence, different array layouts, and larger WEC farms remains to be further investigated.

CRediT authorship contribution statement

Yi Zhang: Writing – review & editing, Writing – original draft, Visualization, Validation, Software, Methodology, Investigation, Conceptualization. **Qian Li:** Validation, Software, Investigation. **Shiqiang Yan:** Writing – review & editing, Supervision, Software, Resources, Funding acquisition, Conceptualization. **Qingwei Ma:** Writing – review & editing, Supervision, Resources, Project administration, Funding acquisition.

Declaration of competing interest

The authors declare that they have no known competing financial interests or personal relationships that could have appeared to influence the work reported in this paper.

Acknowledgements

The authors gratefully acknowledge the financial support of EPSRC projects (Grant Nos. EP/V040235/1, EP/T026782/1, EP/V039946/1 and EP/T00424X/1).

Appendix A. Mesh deformation using different scale functions

Fig. A1 compares the mesh deformation around two CorPower buoys using different scale functions at the same time instant.

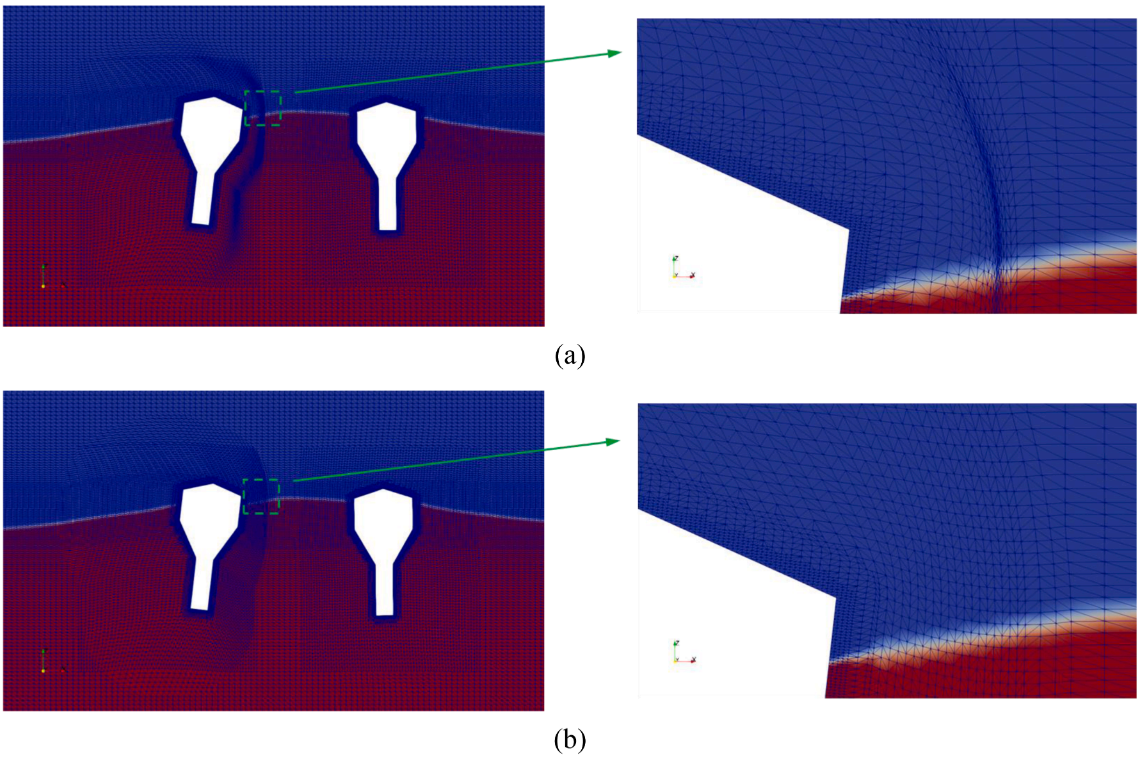

Fig. A1. Comparison of mesh deformation around two CorPower buoys at the same time instant using different scale functions. (a) Cosine-type scale function; (b) Hybrid scale function.

Appendix B. Boundary absorption assessment

To provide additional evidence for the boundary treatment in the multi-buoy setting, we have added a numerical cross-check for a representative two-buoy case with the wave period $T = 2.25$ s and the wave height $H = 0.36$ m. The results obtained using the improved self-adaptive wave absorbing technique are compared with those from conventional relaxation-zone implementation, as shown in Fig. B1 and Fig. B2. The conventional relaxation-zone setup requires a 10 m-long computational domain, including two 2.0 m-wide relaxation zones placed at the two ends of the NS domain, and approximately 2.5 million cells. In comparison, the present wave-absorber treatment requires only a 6 m-long computational domain with approximately 1.7 million cells. This corresponds to reductions of 40% in domain length and approximately 32% in cell count. The comparison shows good agreement in the buoy motion responses, indicating that the present boundary treatment does not introduce noticeable reflection effects for the considered multi-buoy configuration. However, the improved self-adaptive wave absorber leads to a substantial reduction in computational cost, with an expected reduction in computational time of approximately 25–35%, depending on the parallel efficiency and load balancing.

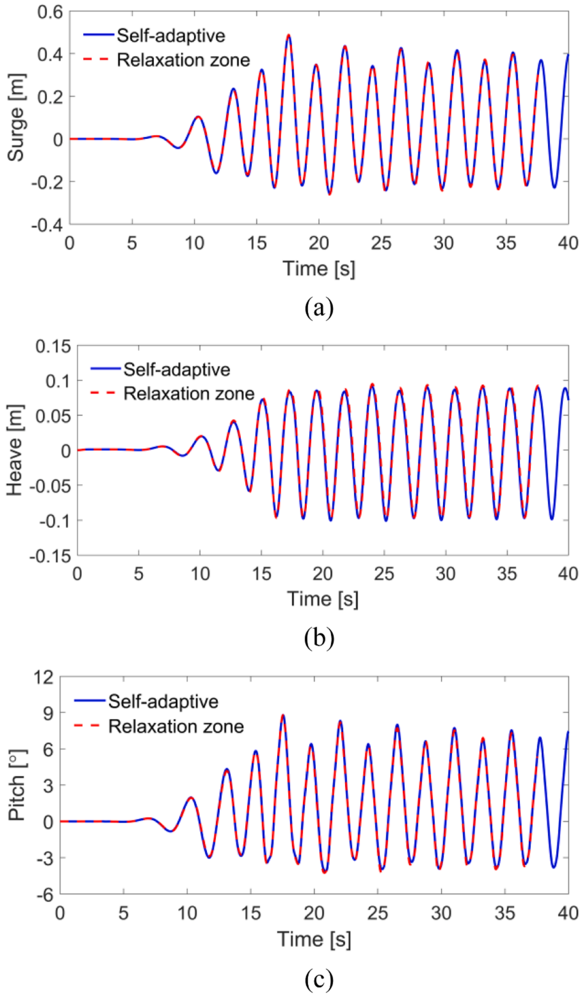

Fig. B1. Comparisons of Buoy 1 motion responses between the present wave-absorber technique and the conventional relaxation-zone implementation for a representative two-buoy case. (a) Surge; (b) Heave; (c) Pitch.

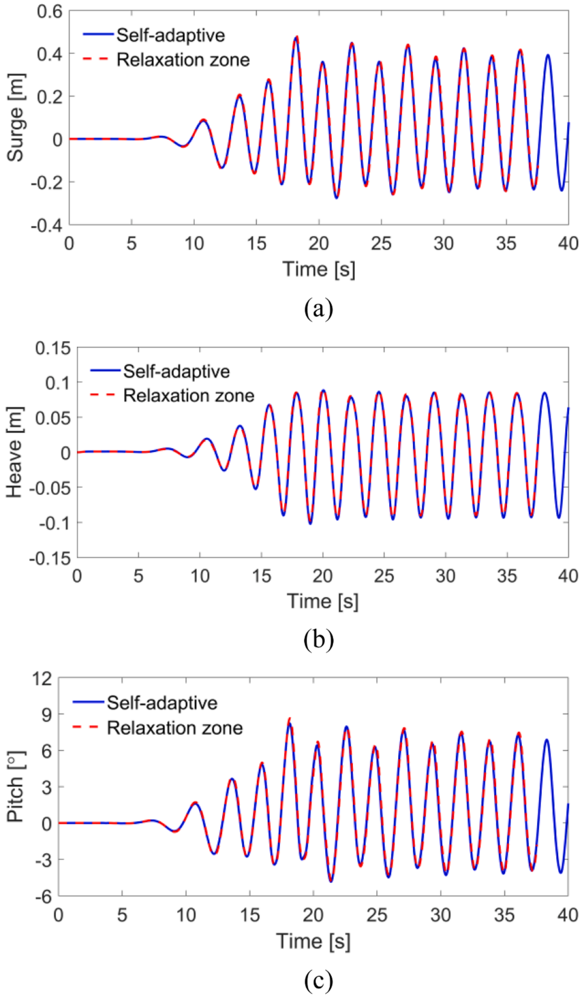

Fig. B2. Comparison of Buoy 2 motion responses between the present wave-absorber technique and the conventional relaxation-zone implementation for a representative two-buoy case. (a) Surge; (b) Heave; (c) Pitch.

References

Aliyar, S., Ducrozet, G., Bouscasse, B., Sriram, V., Ferrant, P., 2022. Efficiency and accuracy of the domain and functional decomposition strategies for the wave-structure interaction problem. Ocean Eng. 266, 112568.
Babarit, A., 2013. On the park effect in arrays of oscillating wave energy converters. Renew. Energy 58, 68–78.
Babarit, A., 2015. A database of capture width ratio of wave energy converters. Renew. Energy 80, 610–628.
Babarit, A., Hals, J., Muliawan, M.J., Kurniawan, A., Moan, T., Krokstad, J., 2012. Numerical benchmarking study of a selection of wave energy converters. Renew. Energy 41, 44–63.
Berberović, E., van Hinsberg, N.P., Jakirlić, S., Roisman, I.V., Tropea, C., 2009. Drop impact onto a liquid layer of finite thickness: dynamics of the cavity evolution. Phys. Rev. E 79, 036306.
Budal, K., 1977. Theory of absorption of wave power by a system of interacting bodies. J. Ship Res. 21 (4), 248–254.
Budal, K., Falnes, J., 1975. A resonant point absorber of ocean-wave power. Nature 256, 478–479 (With Corrigendum in vol. 257, pp. 626).
Chandar, D.D., 2019. On overset interpolation strategies and conservation on unstructured grids in OpenFOAM. Comput. Phys. Commun. 239, 72–83.
Chen, H., Liang, H., Lin, Z., Li, Y., Shi, W., 2025. Hydrodynamic and energy-harvesting performance of an array of taut-moored point-absorber wave energy converters. Energy 337, 138546.
Chen, H., Qian, L., Ma, Z., Bai, W., Li, Y., Causon, D., Mingham, C., 2019. Application of an overset mesh based numerical wave tank for modelling realistic free-surface hydrodynamic problems. Ocean Eng. 176, 97–117.
Child, B., Venugopal, V., 2010. Optimal configurations of wave energy device arrays. Ocean Eng. 37, 1402–1417.
Davidson, J., Costello, R., 2020. Efficient nonlinear hydrodynamic models for wave energy converter design–a scoping study. J. Mar. Sci. Eng. 8, 35.
Devolder, B., Rauwoens, P., Troch, P., 2017. Towards the numerical simulation of 5 floating point absorber wave energy converters installed in a line array using OpenFOAM. In: Proc. 12th Eur. Wave Tidal Energy Conf., Cork, Ireland.
Evans, D.V., 1979. Some theoretical aspects of three dimensional wave energy absorbers. In: Proc. 1st Symp. Ocean Wave Energy Utilization, Gothenburg, Sweden.
Falcão, AFdeO, 2010. Wave energy utilization: a review of the technologies. Renew. Sustain. Energy Rev. 14 (3), 899–918.
Falnes, J., 1980. Radiation impedance matrix and optimum power absorption for interacting oscillators in surface waves. Appl. Ocean Res. 2, 75–80.
Falnes, J., 2007. A review of wave-energy extraction. Mar. Struct. 20 (4), 185–201.

Falnes, J., 2002. Ocean Waves and Oscillating Systems: Linear Interactions Including Wave-Energy Extraction. Cambridge University Press, Cambridge, UK.
Folley, M., Babarit, A., Child, B., Forehand, D., O'Boyle, L., Silverthorne, K., Spinneken, J., Stratigaki, V., Troch, P., 2012. A review of numerical modelling of wave energy converter arrays. In: Proc. ASME 31st Int. Conf. Ocean, Offshore Arct. Eng., Rio de Janeiro, Brazil, 7, pp. 535–545.
Gong, J.Y., Yan, S., Ma, Q.W., Li, Y.B., 2020. Added resistance and seakeeping performance of trimarans in oblique waves. Ocean Eng. 216, 107721.
He, G., Luan, Z., Zhang, W., He, R., Liu, C., Yang, K., Yang, C., Jing, P., Zhang, Z., 2023. Review on research approaches for multi-point absorber wave energy converters. Renew. Energy 218, 119237.
Jacobsen, N.G., Fuhrman, D.R., Fredsøe, J., 2012. A wave generation toolbox for the open-source CFD library: OpenFoam. Int. J. Numer. Meth. Fluids 70 (9), 1073–1088.
Jin, S., Patton, R.J., Guo, B., 2018. Viscosity effect on a point absorber wave energy converter hydrodynamics validated by simulation and experiment. Renew. Energy 129, 500–512.
Kagemoto, H., Yue, D.K.P., 1986. Interactions among multiple three-dimensional bodies in water waves: an exact algebraic method. J. Fluid Mech 166, 189–209.
Li, Q., Wang, J.H., Yan, S., Gong, J.Y., Ma, Q.W., 2018. A zonal hybrid approach coupling FNPT with OpenFOAM for modelling wave-structure interactions with action of current. Ocean Syst. Eng. 8 (4), 381–407.
Li, Y., Yu, Y.H., 2012. A synthesis of numerical methods for modeling wave energy converter-point absorbers. Renew. Sustain. Energy Rev. 16 (6), 4352–4364.
Liu, Y., 2019. HAMS: a frequency-domain preprocessor for wave-structure interactions—theory, development, and application. J. Mar. Sci. Eng. 7, 81.
Liu, Y., Zheng, S., Liang, H., Cong, P., 2022. Wave interaction and energy absorption from arrays of complex-shaped point absorbers. Phys. Fluids 34, 097107.
Ma, Q.W., Yan, S., 2006. Quasi ALE finite element method for nonlinear water waves. J. Comput. Phys. 212 (1), 52–72.
Ma, Q.W., Yan, S., 2009. QALE-FEM for numerical modelling of non-linear interaction between 3D moored floating bodies and steep waves. Int. J. Numer. Meth. Eng. 78 (6), 713–756.
McCallum, P.D., 2017. Numerical Methods for Modelling the Viscous Effects on the Interactions Between Multiple Wave Energy Converters. The University of Edinburgh. Doctoral thesis.
OpenFOAM, 2017. OpenFOAM version 5.0 user guide. https://cfd.direct/openfoam/user-guide.
Orszaghova, J., Wolgamot, H., Draper, S., Eatock Taylor, R., Taylor, P.H., Rafiee, A., 2019. Transverse motion instability of a submerged moored buoy. Proc. R. Soc. A 475, 20180459.
Paulsen, B.T., Bredmose, H., Bingham, H.B., 2014. An efficient domain decomposition strategy for wave loads on surface piercing circular cylinders. Coast. Eng. 86, 57–76.
Schäffer, H.A., 1996. Second-order wavemaker theory for irregular waves. Ocean Eng. 23 (1), 47–88.
Todalshaug, J.H., Ásgeirsson, G.S., Hjálmarsson, E., Maillet, J., Möller, P., Pires, P., Guérinel, M., Lopes, M., 2016. Tank testing of an inherently phase-controlled wave energy converter. Int. J. Mar. Energy 15, 68–84.
Wang, W., Wu, M., Palm, J., Eskilsson, C., 2018. Estimation of numerical uncertainty in computational fluid dynamics simulations of a passively controlled wave energy converter. Proc. IMechE Part M: J. Eng. Marit. Environ. 232 (1), 71–84.
Windt, C., Davidson, J., Chandar, D.D., Faedo, N., Ringwood, J.V., 2020. Evaluation of the overset grid method for control studies of wave energy converters in OpenFOAM numerical wave tanks. J. Ocean Eng. Mar. Energy 6 (1), 55–70.
Windt, C., Davidson, J., Ringwood, J.V., 2018. High-fidelity numerical modelling of ocean wave energy systems: a review of computational fluid dynamics-based numerical wave tanks. Renew. Sustain. Energy Rev. 93, 610–630.
Windt, C., Davidson, J., Schmitt, P., Ringwood, J.V., 2019. On the assessment of numerical wave makers in CFD simulations. J. Mar. Sci. Eng. 7 (2), 47.
Wolgamot, H.A., Fitzgerald, C.J., 2015. Nonlinear hydrodynamic and real fluid effects on wave energy converters. Proc. IMechE Part A: J. Power and Energy 229 (7), 772–794.
Wolgamot, H.A., Taylor, P.H., Eatock Taylor, R., 2012. The interaction factor and directionality in wave energy arrays. Ocean Eng. 47, 65–73.
Yan, S., Ma, Q.W., 2010a. QALE-FEM for modelling 3D overturning waves. Int. J. Numer. Meth. Fluids 63 (3), 743–768.
Yan, S., Ma, Q.W., 2010b. Numerical simulation of interaction between wind and 2D freak waves. Eur. J. Mech. B Fluids 29 (1), 18–31.
Yan, S., Ma, Q.W., Wang, J.H., Zhou, J.T., 2016. Self-adaptive wave absorbing technique for nonlinear shallow water waves. In: Proc. ASME 35th Int. Conf. Ocean Offshore Arct. Eng., Busan, South Korea.
Yan, S., Wang, J.H., Wang, J.X., Ma, Q.W., Xie, Z., 2020. CCP-WSI blind test using qaleFOAM with an improved passive wave absorber. Int. J. Offshore Polar Eng. 30 (1), 43–52.
Yu, Y.H., Li, Y., 2013. Reynolds-averaged Navier-Stokes simulation of the heave performance of a two-body floating-point absorber wave energy system. Comput. Fluids 73, 104–114.
Zhang, Y., Teng, B., Gou, Y., 2021. Nonlinear modelling of a point-absorber wave energy converter based on the weak-scatterer approximation. Ocean Eng. 239, 109924.